

RESEARCH ON PRIME-FOCUS FEEDS

Rastislav Galuščák⁽¹⁾, Pavel Hazdra⁽¹⁾, Miloš Mazánek⁽¹⁾

⁽¹⁾Czech Technical University, FEE, Dept. of Electromagnetic Field, Prague, Czech Republic,
Email: om6aa@yahoo.com, hazdrap@fel.cvut.cz, mazanekm@fel.cvut.cz

INTRODUCTION

The requirements of the Geophysical Institute of the Academy of Science of Czech Republic on new primary feeds for weak signal reception from science satellites, initiated cooperation and common development of the new prime-focus feeds with higher efficiency for existing dish antennas. The other motivation of the feeds design was for amateur radio microwave “Earth-Moon-Earth” (Moon Bounced) communication, using the Moon as a passive microwave reflector.

SEPTUM POLARIZERS

Systematic design of primary feeds equipped with septum polarizer for satellite reception and also for EME (Earth-Moon-Earth) use has been started within our department four years ago. The following one (Fig. 1) [1], [2] works in 1296MHz (23cm) band with excellent properties: RL better than -30dB and isolation between ports 26dB (Fig. 1). This septum polarizer was implemented for various frequencies and also for different f/D ratio of the dish reflector. Polarization efficiency has been evaluated by integrating the simulated RHC and LHC farfields to obtain radiated powers (cons). This septum yields $\eta_{pol}=97.7\%$.

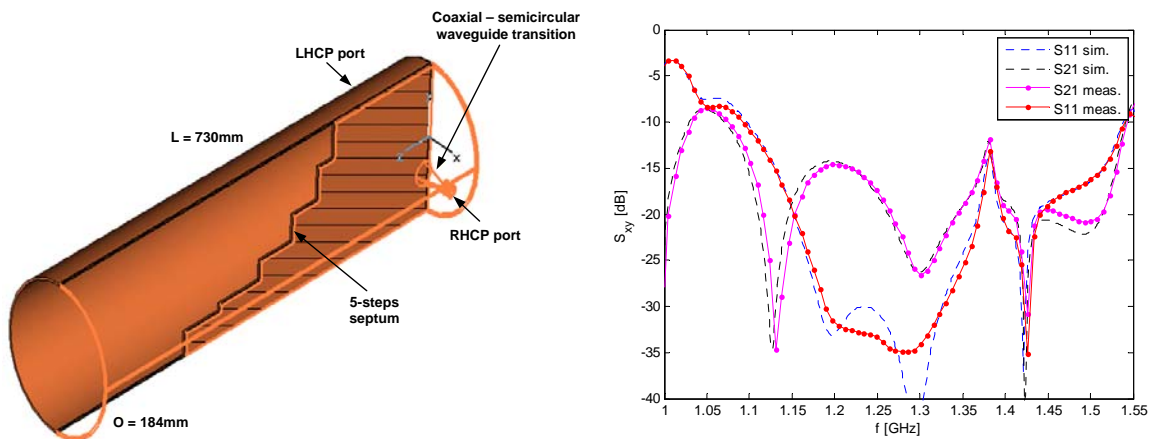


Fig. 1. Proposed septum feed layout and comparison of simulated and measured S-parameters

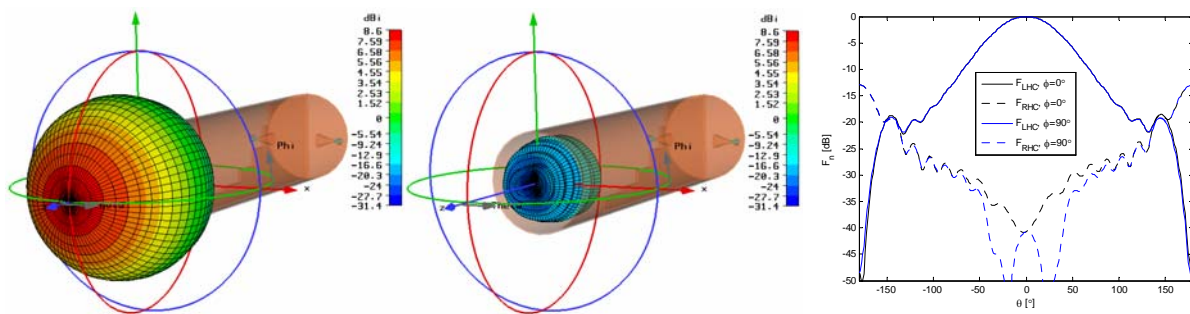


Fig. 2. Simulated 3D directivity pattern @ 1296 MHz with LHC port excited, RHC component shown. Pattern is normalized to maximum directivity of the main RHC component ($D_{max}=8.61$ dBi). LHC pattern (left), RHC (middle). Pattern cuts for both polarizations (right)

Septum Polarizer with Dual Mode Aperture Field Distribution

This feed was developed for dishes with f/D ratio 0.4 up to 0.5. While the septum polarizer is placed in waveguide with inner diameter 0.8λ , to excite higher mode TM_{11} conical section with waveguide 1.3λ diameter and appropriate length was added (Fig. 3). The achieved results are excellent. Back radiation is suppressed better than 30 dB and axial ratio for boresight transmission is better than 0.6 dB.

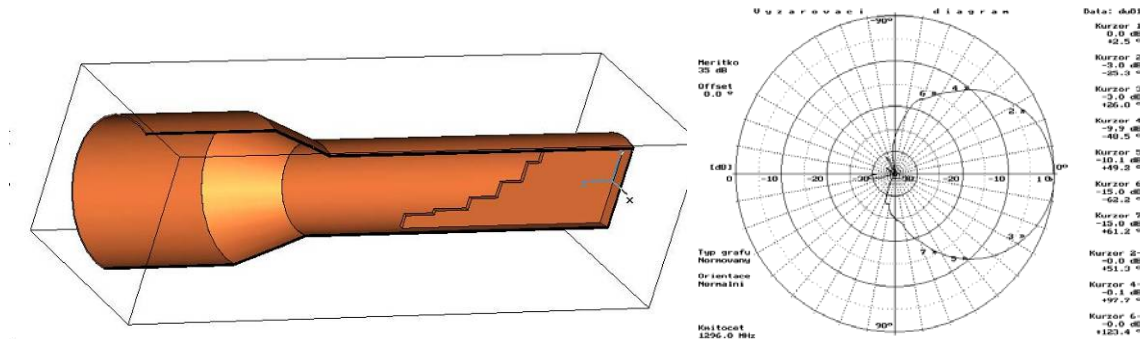


Fig. 3. Dual mode feed with septum polarizer and its radiation pattern cut

Feeds for 13 and 6 cm Band

Our designed 23cm feed was scaled and adapted for 13 and 6 cm bands. The requirement for 13 cm band was to achieve good wide band parameters, at least 10% bandwidth. To meet this criteria, new optimization in MICIAN and CST-MWS [3] was performed. The most monitored parameter was S_{21} port-to-port isolation. The results are shown in Fig.4.

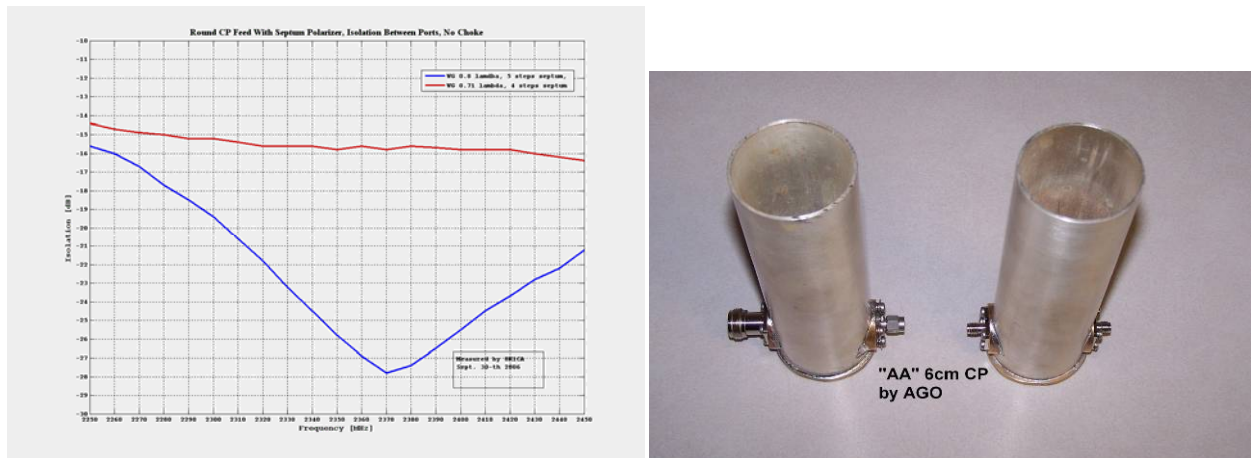


Fig. 4. S_{21} parameters of 13cm feed (left) and 6cm feed built sample (right)

PRIME-FOCUS FEED WITH BACKWARD RADIATION

Recent work at the department is the design of a prime-focus feed for a 60cm diameter parabolic dish antenna with f/D ratio 0.285 (subtended angle 171°) for a frequency of 10.368 GHz. The main advantage of this feed configuration is improved dish antenna efficiency with a very simple mechanical setup; the design was inspired by work [4]. Design goals were:

- Linear / circular polarization capabilities
- Good axial ratio (with CP)
- Low cross-polarization losses
- -13 dB dish edge taper for low side lobes + pattern formation to minimize blockage effects

The feed consists of a relatively small number of parts (Fig. 5): Dielectric Teflon lens with conical cap, circular waveguide, Teflon transition with tuning hole and metal reflecting plate.

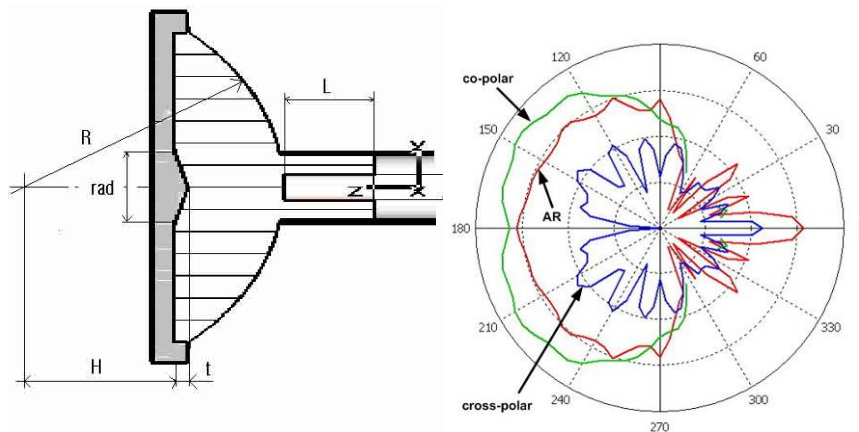


Fig. 5. Feed design and calculated radiation pattern cuts for CP

For linear polarization measurements, a very simple coaxial-to-waveguide transition consisting of the inner pin of a SMA connector positioned within the circular waveguide was used. This transition was tuned for best impedance match at 10.368GHz. Relative bandwidth of the entire feed in free space is approximately 3% for $S_{11} < -20\text{dB}$. The feed assembly was measured in an anechoic chamber and E/H plane cuts were evaluated. See Fig. 6. Excellent agreement between modeled and measured parameters was observed.

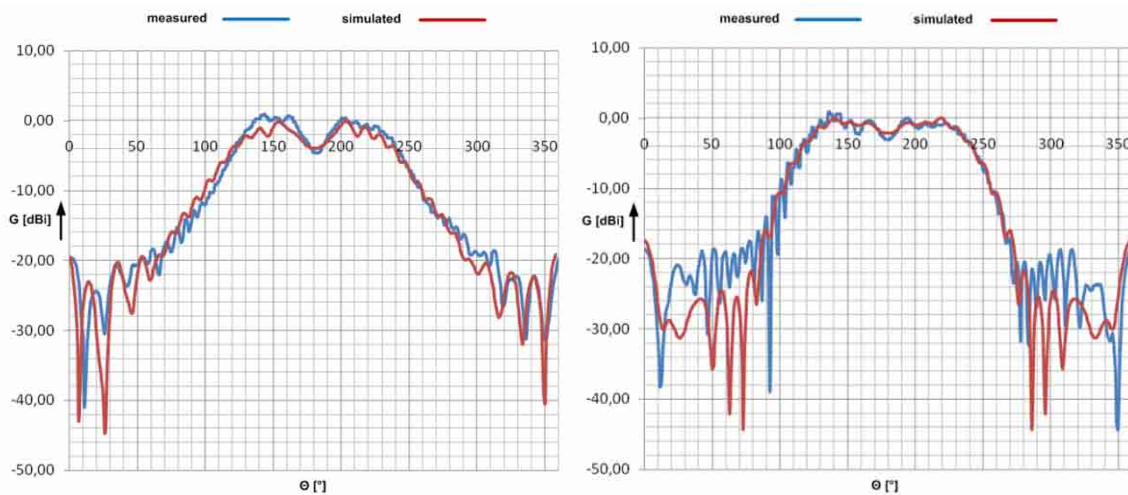


Fig. 6. Calculated and measured radiation pattern cuts for linear polarization (E-plane left, H-plane right)

DESIGN OF PRIMARY FEEDS FOR 32 m KDDI ANTENNA CASSEGRAIN SYSTEM

A proposal for using the KDDI 32-meter Cassegrain reflecting dish antenna (see Fig.7) for amateur radio EME (Earth-Moon-Earth microwave communication utilizing the Moon as a passive reflector) was initiated in 2006 when a group of Japanese amateur radio enthusiasts met for their special meeting at KDDI-Ibaraki Satellite Communication Center in Takahagi City, Japan. At the present time, not all KDDI antennas are in active service; some being in stand-by mode. This resulting availability of “antenna time” along with a favorable approval from KDDI fostered creation of amateur radio’s “Project Big Dish”, whose charter was to communicate on the 144 (2m), 432 (70cm), 1296 (23cm) and 5760 (6cm) MHz amateur radio bands. A special license and call sign, 8N1EME, was issued by the Japanese Telecommunication Authorities for this event. A special taskforce consisting of 40 Japanese radio amateurs was formed to solve the associated technical and logistic problems. Later, engineers from CTU-FEE in Prague were invited into the team for consulting and designing the 2m, 70cm and 23cm primary feeds [5].



Fig. 7. 32m-diameter KDDI Antenna System IBA-4 and 23cm band feeding system assembly (septum feed+dish)

A model of the KDDI Cassegrain antenna system was created using ICARA software. Antenna models for FEKO and CST MWS were also created for additional computations and optimization of the antenna system.

The main parts designed were:

- Primary septum-polarizer feed for 23cm (1296MHz) band with additional dish antenna (Fig. 7)
- Feeds for 70cm and 2m bands using two 1λ loops placed close to the main dish subreflector

Summary of the designed system:

- 23cm (1296MHz) band efficiency: 53%, $\sim 50\text{dBi}$
- 70cm (434MHz) band efficiency: 13%, $\sim 34\text{dBi}$
- 2m (144MHz) band efficiency: 31%, $\sim 29\text{dBi}$

From practical point of view, the 8N1EME station successfully worked with 154 stations on the 2 m band, 67 stations on 70 cm and 71 stations on 23 cm. We had the opportunity to design, fabricate, test and use an antenna system based on the KDDI Cassegrain antenna, and transformed it into a multiband antenna touting a unique *triple* reflector configuration on the 23 cm band! More details could be found at [5].

ACKNOWLEDGEMENT

The research is a part of the COST IC 0603 ASSIST activities and was supported partly by project of the Ministry of Education, Youth and Sports of the Czech Republic, “Antenna Systems and Sensors with special Properties”. The final version of the illuminator was tested due to the 8N1EME station activities in Japan. The authors thank to the CST Microwave Studio for help and advice with computer simulations.

REFERENCES

- [1] R. Galuscak, P. Hazdra, “Prime-focus Circular Waveguide Feed with Septum Polarization Transformer”. *DUBUS - Magazine for Amateur Radio on VHF/UHF and Microwaves*, vol. 36, no. 1, pp. 8-32. ISSN 1438-3705, 2007
- [2] P. Hazdra, R. Galuscak, M. Mazanek, “Optimization of the Septum Polarizer Feed for 1.296 GHz EME”, *Proceedings of the EuCAP 2006* [CD-ROM]. Noordwijk: ESA Publications Division, ISBN 92-9092-937-5, 2006
- [3] CST Microwave Studio, www.cst.com
- [4] P. S. Kildal, T. Jensen, “Efficient small reflector with hat feed”, *ICAP, Antennas and Propagation*, vol. 1, no. 301, pp. 154-157, 1989
- [5] R. Galuscak, M. Watanabe, P. Hazdra, S. Takeda, K. Seki, M. Prochazka, Y. Uchiyama, “Design of Primary Feeds for 32m KDDI Antenna System IBA-4 in Cassegrain Config.”, *Radioengineering*, vol. 14, no. 1, pp. 20-28, 2008

RECONFIGURABLE ANTENNAS BY RF MEMS TECHNOLOGY

Kagan Topalli, Omer Bayraktar, Mehmet Unlu, Ozlem Aydin Civi, Simsek Demir, and Tayfun Akin

Middle East Technical University, Dept. of Electrical and Electronics Eng., Ankara, Turkey, kagan@metu.edu.tr

INTRODUCTION

MEMS technology is a powerful way of merging the functions of sensing and actuation with computation and communication to control physical parameters at the microscale. Present markets of MEMS technology are mainly in pressure and inertial sensors, inkjet print heads, and high-resolution digital displays. Future and emerging applications include tire pressure sensing, fiber optical components, fluid management and processing devices for chemical microanalysis, medical diagnostics, and drug delivery, and RF and wireless electronics, namely RF MEMS. The application of MEMS technology to RF systems enables production of components with low power consumption, high linearity, low insertion loss, and high isolation. RF MEMS components are particularly attractive for researchers due to their tunable properties. This technology is used to implement many tunable circuits and systems in a miniaturized way that has never been implemented before using any other technology [1].

With the development of advanced commercial and military microwave systems and applications, there is a growing need for a single antenna that can be operated at different frequencies, where each of these frequencies are tunable. For example, an antenna whose resonant frequency can be tuned continuously in a frequency range can be used in radar applications for frequency hopping. A tunable antenna can also be used in telecommunications to maintain different system frequencies. Another application area of such antennas is satellite communications systems, where one operating frequency is used for the transmitter and the other for the receiver. There is a need for monolithic implementation of such antennas to reduce the system size, parasitic coupling between radiators, system complexity, and cost.

Monolithic implementation of various antennas and components has become possible with the MEMS technology. The MEMS technology and its application to RF systems enable production of tunable components such as switches, capacitors, and matching networks with low power consumption, high linearity, and high performance [1]. RF MEMS tunable circuit elements make the realization of reconfigurable antenna structures more efficiently in terms of lower insertion losses and lower volumes. Also, the monolithic fabrication of the antenna together with these tunable components reduces the power losses and parasitic effects compared to hybrid integration of antennas with discrete components. It has been shown in literature that MEMS switches and MEMS tunable capacitors are used in reconfigurable antennas to control the resonant frequency, bandwidth, polarization, and radiation pattern [2], [3].

This paper presents the RF MEMS reconfigurable antennas designed and produced in METU using the in-house fabrication process developed at the Microelectronics Facilities. The next sections presents the frequency tunable slot antenna, frequency tunable patch antenna, the monolithic phased array, and the RF MEMS fabrication flow developed at METU.

FREQUENCY TUNABLE PATCH ANTENNA

Fig. 1 shows the frequency tunable patch antenna designed and fabricated at METU. The structure consists of a patch antenna loaded with a coplanar waveguide (CPW) loading section attached to the antenna via microstrip to CPW transition. The reconfigurability in the resonant frequency of the antenna is provided with the aid of the MEMS bridges acting as a variable capacitor placed on the CPW stub [3]. MEMS capacitors are electrostatically actuated with a low tuning voltage in the range of 0-11.9 V. The antenna resonant frequency can continuously be shifted from 16.05 GHz down to 15.75 GHz as the actuation voltage is increased from 0 to 11.9 V. These measurement results are in good agreement with the simulation results obtained with Ansoft HFSS as given in Fig. 1 (b).

DUAL-FREQUENCY RECONFIGURABLE SLOT DIPOLE ARRAY

This section of the paper presents a 4-element linear array of dual-frequency slot dipole antennas whose resonant frequencies are controlled via MEMS switches placed on the slots. Fig. 2 shows the schematic view of the dual-frequency array. The operation frequencies are selected as 10 and 16 GHz so that the system can be fitted into a 500 μm -thick 4" glass substrate. The distance between phase centers of antennas are 1.8 cm to avoid grating lobe for

both frequencies. The slot dipole antennas can either be operated at 10 GHz or 16 GHz with the aid of RF MEMS switches located on the slot arms. The feed network includes 50 Ω -100 Ω dual-frequency transformers, chamfered CPW right-angle bends and T-junctions. Fig. 3 (a) and (b) shows the fabricated prototypes of the slot antennas on a duroid substrate, where metallic strips are employed in order to model the switches in the up and downstate. Fig. 3 (c) gives the measured and simulated reflection coefficients values of the prototype antennas.

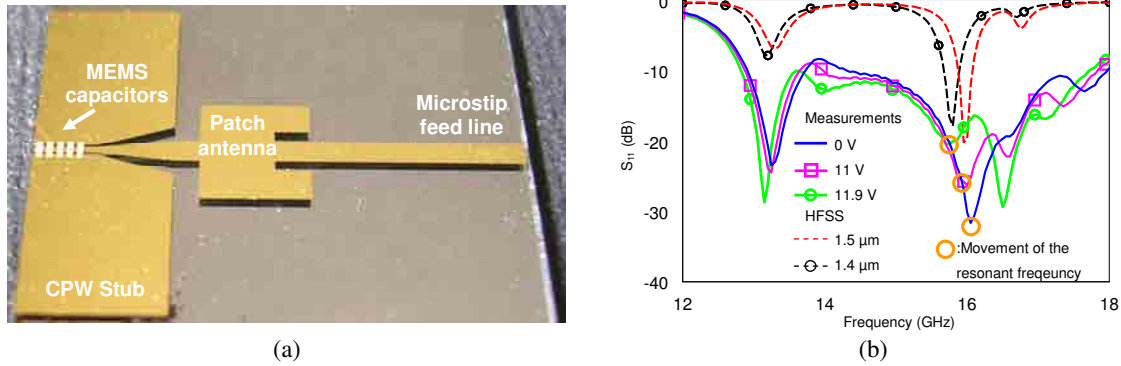


Fig. 1. (a) The photograph of the patch antenna loaded with MEMS capacitors. (b) The measurement results of the patch antenna for different actuation voltages.

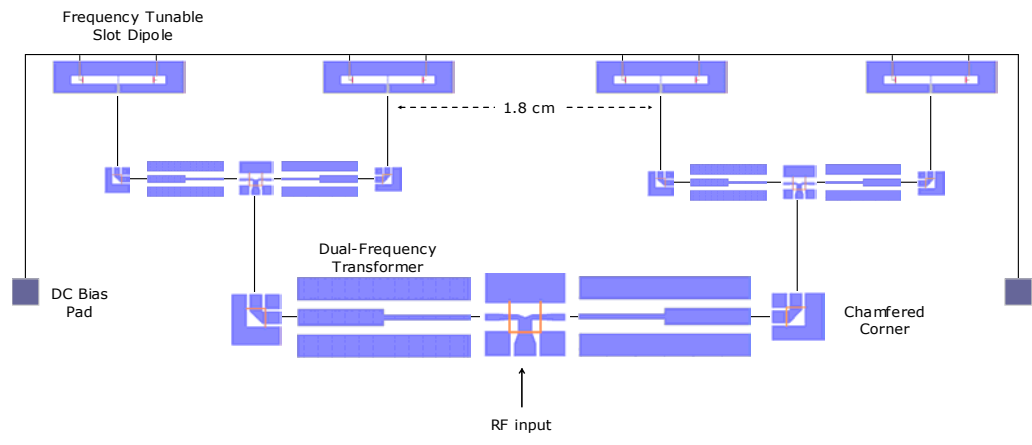


Fig. 2. The schematic view of the dual-frequency array.

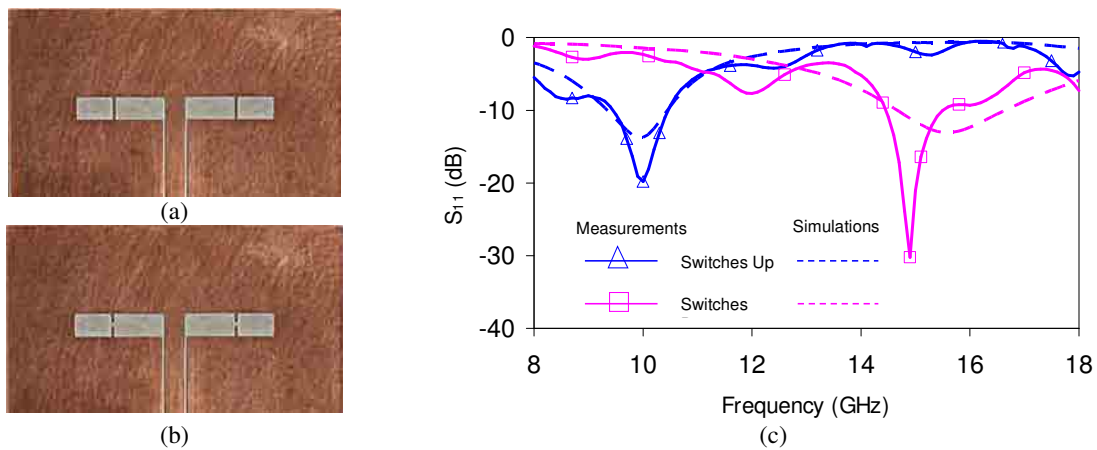


Fig. 3. Fabricated prototypes of the slot antennas and measurement results: (a) switches up, (b) switches down, and (c) measured and simulated performances of the prototype antennas.

MONOLITHIC PHASED ARRAY

This section presents the phased array system designed at 15 GHz employing 3-bit Distributed MEMS transmission line (DMTL) type phase shifters which are monolithically integrated with the feed network of the system and the radiating elements on the same substrate [7]. The phase shifters of the phased array include a total of 128 switches. The phase shifter can give 0° - 360° phase shift with 45° steps at 15 GHz which is used to obtain various combinations of progressive phase shift in the excitation of radiating elements. The phased array is composed of four linearly placed microstrip patch antennas. Fig. 4 shows the photograph of the phased array fabricated on a glass substrate. The digital phase shifter used in the system is composed of a periodically loaded high-impedance transmission line ($> 50 \Omega$) with MEMS bridges in series with lumped capacitors, forming a DMTL. Fig. 5 (a) shows the measured inserted phase shifts for different state. Fig. 5 (b) shows the measured radiation pattern results for different progressive phase shift. The main beam can be steered by 4° , 14° as the phase shifter states are adjusted accordingly. To the authors' knowledge this work is one of the first few monolithically fabricated electronically scanning phased array systems employing large amount of RF MEMS components, reported in the literature.

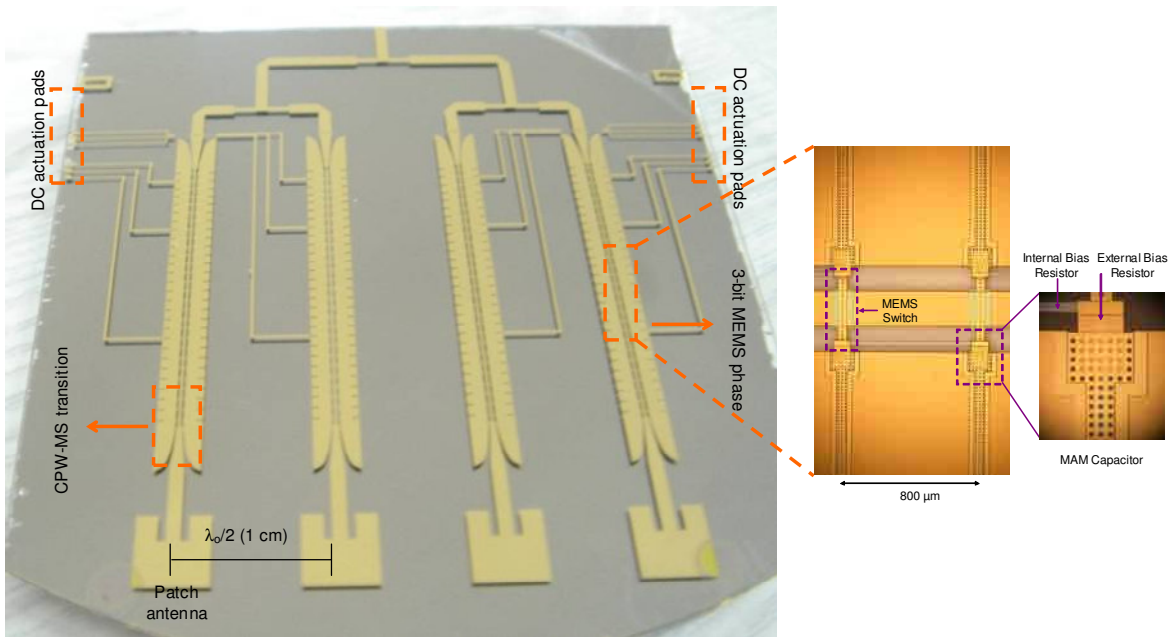


Fig. 4. (a) Photograph of the fabricated phased array. Total chip size is about $6 \text{ cm} \times 5 \text{ cm}$.

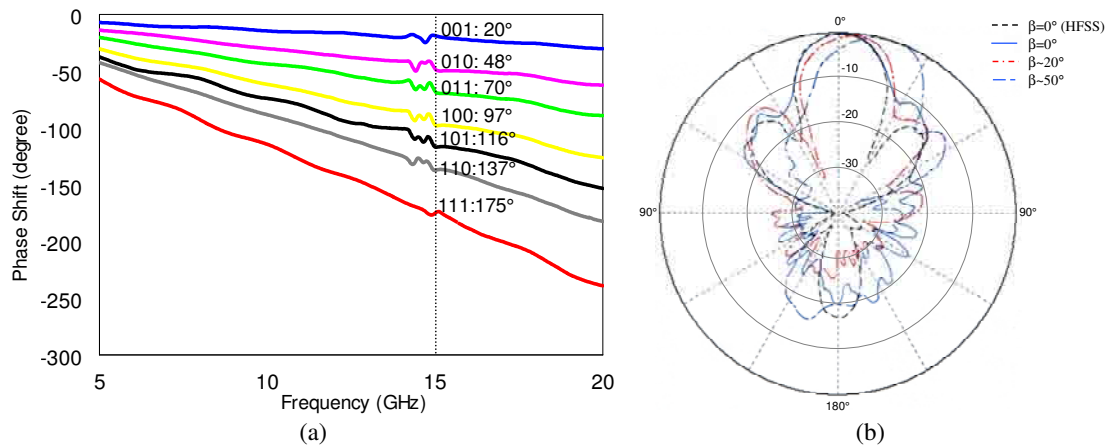


Fig. 5. (a) Measured phase shift vs. frequency plot obtained for 8 states of the 3-bit RF MEMS phase shifter, (b) Measured radiation pattern of the monolithic phased array for different settings of the phase shifters.

FABRICATION PROCESS

Fig. 6 shows the fabrication process developed at METU Microelectronics Facilities. The process starts with sputtering of a 100/3000-Å thick Ti/Au layer, which is required as the seed layer for electroplating of the base metallization. The base metallization layer is formed using a 2-µm thick gold layer, which is electroplated inside the regions defined by the mold photoresist. The remaining Ti/Au seed layer is etched using wet etchants. A 3000 Å-thick Si₃N₄ layer is coated as the DC isolation layer using plasma enhanced chemical vapor deposition technique (PECVD) and patterned using the reactive ion etching (RIE) technique. The next step is the spin-coating of the photodefinable polyimide, PI 2737, as the 2-µm thick sacrificial layer. Then, a 1-µm thick gold layer is sputter-deposited and patterned. The sacrificial layer is wet etched, rinsed, and dried in a critical point dryer.

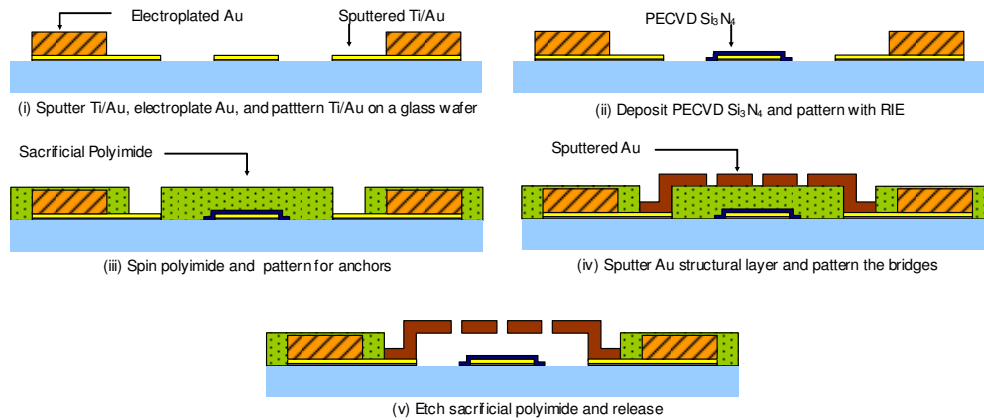


Fig. 6. The process flow used in the fabrication of the reconfigurable antenna structures.

CONCLUSIONS

This paper reviews some examples of reconfigurable antennas designed and fabricated using RF MEMS technology developed at METU. It is shown by the measurement results that the fabricated antennas satisfy the design specifications. More components, as well as production, modeling and packaging studies will be presented and discussed during the presentation in the conference.

ACKNOWLEDGMENT

This research is supported by The Scientific and Technical Research Council of Turkey (TUBITAK-COST IC 0603-107E090, TUBITAK-COST284-102E036, TUBITAK-104E041), Turkish State Planning Organization (DPT), and AMICOM (Advanced MEMS For RF and Millimeter Wave Communications) Network of Excellence under 6th Framework Program of European Union.

REFERENCES

- [1] G. M. Rebeiz, "RF MEMS theory, design, and technology", Hoboken, NJ: John Wiley & Sons, 2003.
- [2] J. C. Chiao, S. -Y. Cheng, J. L. Chang, I. M. Chio, Y. Kang, and J. Hayasaka, "MEMS reconfigurable antennas," *Int. J. RF Microwave CAE*, vol.11, pp. 301-309, 2001.
- [3] E. Erdil, K. Topalli, M. Unlu, O. A. Civi, and T. Akin, "Frequency tunable microstrip patch antenna using RF MEMS technology," *IEEE Transactions on Antennas and Propagation*, vol. 55, pp.1193-1196, April 2007.
- [4] Daniel Llorens, Pablo Otero, and Carlos Camacho-Peñalosa, "Dual-band, single CPW port, planar-slot antenna," *IEEE Trans. on Antennas and Propagation*, vol. 51, pp.137-139, Jan. 2003.
- [5] A.A. Eldek, A.Z. Elsherbeni, C. E. Smith, and K. Lee, "Wideband Rectangular Slot Antenna for Personal Wireless Communication Systems," *IEEE Antennas and Propagation Magazine*, vol. 44, pp.146-155, October 2002.
- [6] E. Erdil, K. Topalli, M. Unlu, I. Istanbuluoglu, E. U. Temocin, H. I. Atasoy, O. Bayraktar, O. A. Civi, S. Demir, S. Koc, and T. Akin, "Reconfigurable slot antenna with fixed-fixed beam type RF MEMS capacitors," in *Proc. Eur. Conf. on Antennas and Propagation*, Nov. 6–10, 2006, on CD.
- [7] K. Topalli, O. Aydin, Civi, S. Demir, S. Koc, and T. Akin, "A Monolithic Phased Array using 3-bit DMTL RF MEMS Phase Shifters," *IEEE Trans. Microwave Theory and Tech.*, vol.56, pp. 270-277, February 2008.

EFFICIENT HYBRID ANALYSIS METHOD OF CURVED FREQUENCY SELECTIVE SURFACES

Marko Bosiljevac and Zvonimir Sipus

University of Zagreb, Faculty of Electrical Engineering and Computing, Croatia
e-mails: zvonimir.sipus@fer.hr, marko.bosiljevac@fer.hr

ABSTRACT

Large curved frequency selective surfaces (FSS) due to the lack of structure periodicity present a very demanding task for an efficient analysis. Proposed hybrid method accomplishes this task by combining rigorous spectral domain approach with a simple and fast free space approach. By implementing free space method into specific parts of the spectral domain algorithm a significant acceleration is achieved in the analysis of electrically large FSS, while retaining sufficient accuracy. This is shown for a spherical FSS composed out of circular ring elements mounted on a thin dielectric supporting structure.

INTRODUCTION

Modern multifrequency reflector systems with frequency selective sub-reflectors can be used in more than one frequency band using only separate feed antennas. This results in significant cost and weight reductions, and reduces the complexity of the overall system. Also, curved FSS present a complete solution for mechanical and electromagnetic protection of radiating objects, or in other words they can be used as frequency selective radomes. However, the main drawback of the curved FSS, the complexity of its analysis still limits the practical applicability of such structures.

Unlike planar FSS that are relatively simple to analyze and for which the analysis tools are commonly included in many commercial electromagnetic solvers, curved FSS present a very serious problem. The reason for this lies in the fact that the periodicity property of the planar FSS, which considerably simplifies its analysis, is lost when analyzing curved FSS. Consequently, the analysis of curved FSS cannot be reduced to the analysis of a single unit cell and basically the entire FSS has to be analyzed at once. Naturally, in order to do that efficiently some kind of simplification or approximation has to be considered.

The obvious solution due to the size of these structures in terms of wavelength is to use a fast high frequency method. Commonly that would mean geometrical optics approach. In this classical approach, a bundle of rays is launched from the source (usually an antenna inside the radome or an antenna exciting a sub-reflector), and each ray is traced forward from the source to the curved FSS. The transmitted ray is determined by considering the transmission coefficient of the equivalent planar FSS and the far field is then obtained by implementing the equivalence principle. The main drawback of this approach is that the transmission through the structure is calculated using the locally planar approximation, ignoring the influence of the curvature and the finiteness of the FSS on its transmission/reflection properties. In order to take these properties into account a more rigorous method has to be applied. Naturally, rigorously considering the entire structure at once would be inefficient for any practical purpose. However, if certain simplifications are introduced into the analysis it is possible to develop a solution much more accurate than the one obtained with the ray approach, and also much faster compared to the rigorous approach itself. This is the idea behind the proposed hybrid method which combines the rigorous spectral domain solution with a simple free space solution in the analysis of curved FSS.

ANALYSIS METHOD

The rigorous analysis approach is based on solving the integral equation for the electric field (EFIE), and on the moment method (MoM), where the elements of the MoM matrix are calculated in the spectral domain. The motivation for applying the spectral domain technique is to transform the three-dimensional problem into a spectrum of one-dimensional problems, which is much easier to solve. Since the considered FSS examples are the spherical ones, the spectrum is obtained by applying the vector-Legendre transformation to the element current [1,2]. The Green's function of a general multilayer spherical structure is computed using the G1DMULT algorithm that calculates spectral domain Green's functions of multilayer planar, circular cylindrical and spherical structures [2].

Unfortunately, such rigorous approach applied to the analysis of electrically large FSS is inefficient due to the fact that the direct computation of mutual coupling terms inside the moment method matrix is very time consuming. This is because the number of the spectral-domain modes needed for accurate calculation of MoM matrix terms is proportional to the structure radius. Furthermore, for each mode a double-integral of rapidly varying functions needs to be evaluated (for large m and n the associate Legendre functions and the exponential functions $\exp(-jm\phi)$ are highly oscillating). If the number of modes could be reduced it would significantly accelerate the analysis procedure.

The basic idea behind the reduction of needed number of modes is to subtract the asymptotic part of the Green's function for the analyzed structure, and to calculate it separately [3]. The so-called asymptotic part carries the major contribution to the overall Green's function and the part left after the subtraction is basically the higher-order mode contribution. In essence this means that the asymptotic part is a rough approximation of the analyzed structure without some fine details, multiple layers etc. The major benefit of this approach is that the asymptotic part because of its "simplicity" can now be calculated using a much simpler method.

To illustrate the concept lets consider the mutual impedance term in the MoM matrix for the spherical FSS:

$$Z_{ji} = - \sum_{m=-\infty}^{\infty} \sum_{n=|m|}^{\infty} r_{ring}^2 \tilde{\mathbf{J}}_j^T(r_{ring}, n, -m) \tilde{\tilde{\mathbf{G}}}(n, m, r_{ring} | r_{ring}) \tilde{\mathbf{J}}_i(r_{ring}, n, m). \quad (1)$$

First we have to extract the asymptotic part and split equation (1) into two parts,

$$\begin{aligned} Z_{ji} = & - \sum_{m=-\infty}^{\infty} \sum_{n=|m|}^{\infty} r_{pt}^2 \tilde{\mathbf{J}}_j^T(r_{pt}, n, -m) \left\{ \tilde{\tilde{\mathbf{G}}}(n, m, r_{pt} | r_{pb}) - \tilde{\tilde{\mathbf{G}}}_{asym}(n, m, r_{pt} | r_{pb}) \right\} \tilde{\mathbf{J}}_i(r_{pb}, n, m) \\ & - \sum_{m=-\infty}^{\infty} \sum_{n=|m|}^{\infty} r_{pt}^2 \tilde{\mathbf{J}}_j^T(r_{pt}, n, -m) \tilde{\tilde{\mathbf{G}}}_{asym}(n, m, r_{pt} | r_{pb}) \tilde{\mathbf{J}}_i(r_{pb}, n, m) \end{aligned} \quad (2)$$

The subtracted part is now independent and no longer has to be calculated in spectral domain; rather it can be solved in spatial domain:

$$\begin{aligned} Z_{ji} = & - \sum_{m=-\infty}^{\infty} \sum_{n=|m|}^{\infty} r_{pt}^2 \tilde{\mathbf{J}}_j^T(r_{pt}, n, -m) \left\{ \tilde{\tilde{\mathbf{G}}}(n, m, r_{pt} | r_{pb}) - \tilde{\tilde{\mathbf{G}}}_{asym}(n, m, r_{pt} | r_{pb}) \right\} \tilde{\mathbf{J}}_i(r_{pb}, n, m) \\ & + \int_{\substack{test \\ function}} \int_{\substack{basis \\ function}} \mathbf{J}_j^T(r_{pt}, \theta, \phi) \tilde{\tilde{\mathbf{G}}}_{asym}(\theta, \phi, r_{pt} | r_{pb}) \mathbf{J}_i(r_{pb}, \theta, \phi) dS dS' \end{aligned} \quad (3)$$

The above formulation illustrates the analysis idea, but the choice of the asymptotic Green's function, which has to be extracted, and the method for its calculation depends on the actual analyzed problem. If considering a FSS with circular ring elements mounted on a thin dielectric sheet it has to be noticed that the actual problem is a multilayered structure consisting out of a central dielectric layer placed between air half-spaces. The dielectric layer is very thin and therefore it is possible to approximate the original problem with a homogeneous space with some effective permittivity. This approximation is actually used for the calculation of the asymptotic part. Since this is a serious simplification, the extracted part can now be calculated using a simple free space Green's function which can be defined as

$$\bar{\mathbf{E}}_j = - \frac{jk}{4\pi} \iint_S \left[\eta \bar{\mathbf{J}} \left(1 + \frac{1}{jkR} \right) - (\eta \bar{\mathbf{J}} \cdot \hat{\mathbf{R}}) \hat{\mathbf{R}} \left(1 + \frac{3}{jkR} - \frac{3}{(kR)^2} \right) \right] \frac{1}{R} e^{-jkR} dS, \quad (4)$$

where $\bar{\mathbf{E}}_j$ is the electric field at a distance R from an electric source $\bar{\mathbf{J}}$ in homogeneous space [4]. The effective permittivity used in this approximation is selected by comparing the resonant frequency of FSS elements placed in the multilayer structure and in the free-space, respectively.

Furthermore, significant reduction in complexity of the spectral-domain analysis part is achieved using a new approach of calculating basis&test functions in the spectral domain. Here two auxiliary potential-like functions \mathbf{A} and ψ are defined as

$$\mathbf{J}_i(r_p, \theta, \phi) = \nabla \times (\hat{r}_p A_r^{J_i}(r_p, \theta, \phi)) + \nabla \cdot (r_p \psi^{J_i}(r_p, \theta, \phi)), \quad (5)$$

and the current in the local (rotated) coordinate system can be found by applying the rotation to these auxiliary functions first, using the Vilenkin's additional theorem for associated Legendre functions [5]:

$$P_n^m(\cos \theta') e^{-jm\phi'} = j^m \sqrt{\frac{(n+m)!}{(n-m)!}} \sum_{k=-n}^n j^{-k} \sqrt{\frac{(n-k)!}{(n+k)!}} P_{m,k}^n(\cos \theta_{12}) P_n^k(\cos \theta) e^{-jk\phi}. \quad (6)$$

The reason why we have defined the auxiliary potential-like functions is that they contain the information about the coordinates only in respective arguments of a product of Legendre and exponential functions. This term can then be transformed from one coordinate system to another by applying the Vilenkin's additional theorem (6). Direct computation of the transform of the rotated element's current would be also very time consuming, because again for every element position a double-integral of rapidly varying functions would have to be evaluated. Details of the proposed method are given in [6].

The curved FSS (i.e. the large finite array) is divided into N subarrays that are separately analyzed using a rigorous full-wave method. Each subarray is locally approximated as a spherical FSS with a local radius of curvature (see Fig. 1) The subarrays have to overlap because the same element in a subarray will have different induced physical or equivalent currents depending on whether it is simulated as an inner element or an edge element, since the edge elements "do not see" the rest of the array environment. The scattered field is calculated as a superposition of the electromagnetic field radiated by the inner parts of N subarrays. This divides an extremely large-scale electromagnetic problem into a sum of simple (small-size) problems and allows the possibility to analyze a general conformal FSS structure using such overlapping subarrays, that is, spherical periodic structures of an appropriate (local) radius of curvature. There are two principles of connecting the subproblems (i.e. the results of the subarray analysis) into a global solution:

1. The current distribution of the elements in the subarray is individually determined. In other words, instead of solving a large MoM matrix equation, one needs to solve a set of small-size MoM matrix equations.
2. The coupling MoM matrices of all subarray problems are connected into a global MoM matrix. The MoM matrix is sparse since large-distance couplings are not taken into account due to subarray approach. Although this approach is more time consuming, it gives more accurate results since all couplings are globally connected (although large-distance couplings are not considered in this approach – they are approximated with zero value).

RESULTS

As an example we have considered an array of circular rings of average radius 2.0 mm (i.e. to the centre of the conductor; the conductor width was 0.4 mm), and separation between ring centres 4.9 mm. The rings are printed on a dielectric substrate of thickness 0.0075 mm and permittivity $\epsilon_r = 2.33$. The rings follow the hexagonal grid (see Fig. 2). The measured resonant frequency of the planar array is around 23 GHz [7]. The transmission coefficient T for the curved FSS with ring elements is defined as the ratio of the magnitude of the total E-field (incident and scattered) at the point z to the magnitude of the E-field due to the incident field alone (i.e. in the absence of the array) $T = \left| \mathbf{E}^{scatt} + \mathbf{E}^{aperture} \right| / \left| \mathbf{E}^{aperture} \right|$. The

incident field $\mathbf{E}^{aperture}$ in the upper expression is calculated as the far field at a distance z in the axial direction radiated by a circular aperture uniformly illuminated with a field of unit amplitude. In the case of curved FSS printed on a dielectric, the influence of the dielectric slab is included in $\mathbf{E}^{aperture}$.

The influence of the structure radius is considered first. We have analyzed the array of 127 elements, i.e. the central element in the array is surrounded with 6 circles of array elements. In order to compare the results with the planar ones, we have considered the structure without dielectric (i.e. rings are placed in the free-space). The structure radius varies from 3.74 cm to 7.48 cm, i.e. from 3.1λ to 6.2λ at the central frequency. It can be seen that for structure radii larger than 4.5λ there is a good agreement between the results for curved and planar FSS – there is only a small shift in resonant frequency present.

The subarray concept is illustrated in Fig. 4. The effective permittivity used in the hybrid method is $\epsilon_{eff} = 1.2$. We have used the second approach of connecting subarrays where all subarray problems are connected into a global MoM matrix. Each subarray consists of a central elements surrounded with 3 circles of elements. It can be seen that there is a small difference in the transmission coefficient magnitude at the resonant frequency, otherwise the agreement is good.

ACKNOWLEDGEMENT: The work reported has been carried out in the framework of COST ASSIST IC0603.

REFERENCES

- [1] W. Y. Tam and K. M. Luk. "Resonances in Spherical-Circular Microstrip Structures of Cylindrical-Rectangular and Wraparound Microstrip Antennas," *IEEE Trans. Microwave Theory Tech.*, **Vol. 39**, pp. 700-704, (1991).
- [2] Z. Sipus, P.-S. Kildal, R. Leijon, and M. Johansson. "An algorithm for calculating Green's functions of planar, circular cylindrical and spherical multilayer substrates", *Appl. Comput. Electromagn. Soc. Journ.*, **Vol. 13**, pp. 243-254, (1998).
- [3] D.M. Pozar, "Improved computational efficiency for the moment method solution of printed dipoles and patches", *Electromagnetics*, Vol. 3, No. 3&4, 1984. pp. 299-309
- [4] P.-S. Kildal, "Foundations of Antennas - A Unified Approach", Studentlitteratur AB, (2000).
- [5] N. Ja. Vilenkin. "Special Functions and the Theory of Group Representation", American Mathematical Society, (1968).
- [6] Z. Sipus, S. Skokic, M. Bosiljevac and N. Burum. "Study of mutual coupling between stacked-patch antennas on a sphere", accepted for publication in *IEEE Trans. on Antennas and Propagat.*
- [7] E.A. Parker, and S.M.A. Hamdy, "Rings as elements for frequency selective surfaces," *Electronics Letters*, **vol. 17**, pp. 612-614, (1981).

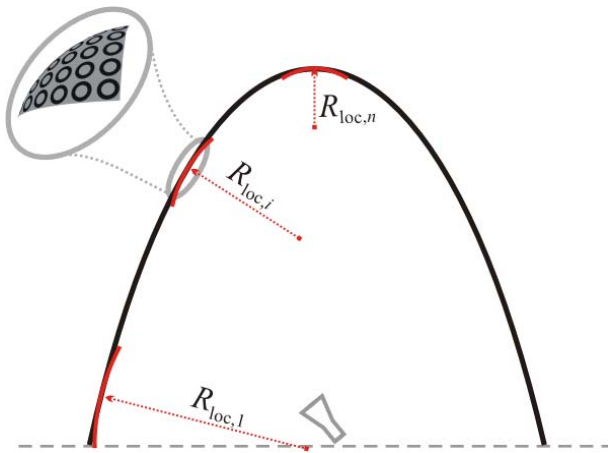


Figure 1. A doubly curved frequency selective radome with circular ring elements. Locally, the curved FSS can be approximated as a spherical FSS.

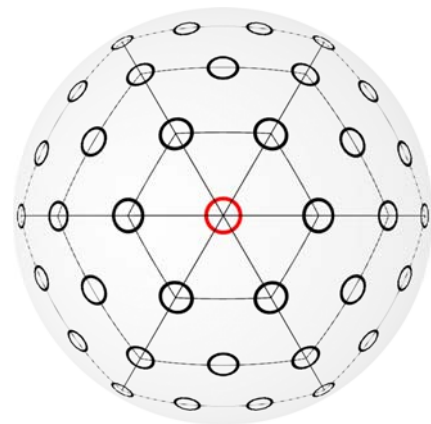


Figure 2. Geometry of the spherical FSS with hexagonal grid.

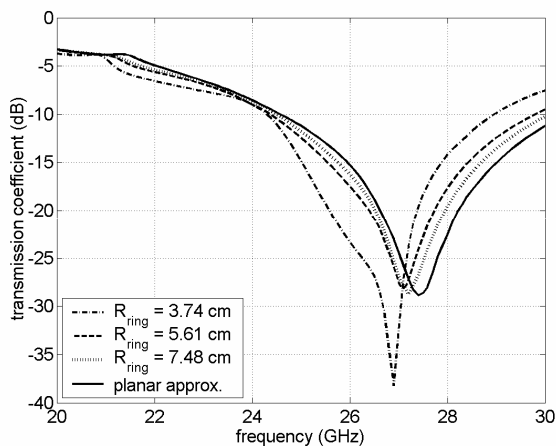


Figure 3. Dependency of the transmission coefficient on the structure radius.

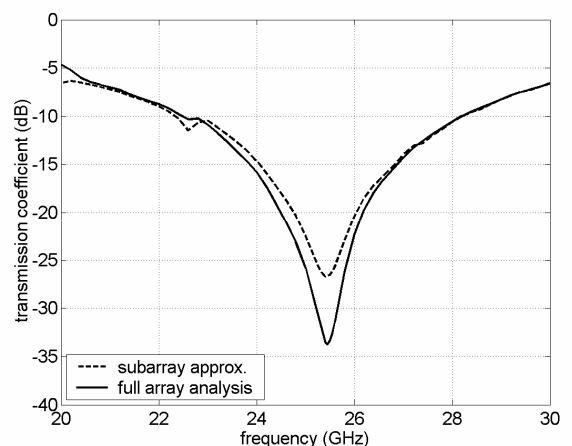


Figure 4. Comparison of the subarray approach of analyzing curved FSS with the full array analysis.

MODELING AND CHARACTERIZATION OF MULTILAYER RADOMES WITH ANISOTROPIC MATERIALS FOR ELECTRONICALLY-SCANNED SATELLITE ANTENNAS

Plamen I. Dankov⁽¹⁾, Vesselin N. Peshlov⁽²⁾, Mario Gachev⁽³⁾

⁽¹⁾University of Sofia, Faculty of Physics, 5, J. Bourchier Blvd., 1164-Sofia, Bulgaria; Email: dankov@phys.uni-sofia.bg

⁽²⁾RaySat BG, Antenna and RF department, 2A, Mogilata Str., 1700-Sofia, Bulgaria, Email: peshlov-v@raysat.bg;

⁽³⁾RaySat BG, Advanced projects, 2A, Mogilata Str., 1700-Sofia, Bulgaria, Email: gachev-m@raysat.bg

ABSTRACT

The paper discusses the problems of the antenna radomes fabricated by anisotropic materials: analytical CAD model, radome measurements, radome simulations and characterisation of the multi-layer radome materials. A modified Paris' model for CAD radome analysis is presented, which takes into account the dielectric material anisotropy of the layers. The model is combined with the two-resonator method for characterization of the normal and parallel to the surface dielectric parameters of the separate radome layers. Useful multi-layer radome simulations and methods for measurement of radome losses are briefly discussed. Finally, an example for Parabeam® 3D-glass radome is given illustrative for implementation of appropriate radome model of reinforced and composite structures with anisotropy. This model takes into account the measured dielectric parameters of all the layers comprising into the given practical radome construction – cores, skins, irregular epoxy glue fillets, protective coatings, 3D layers, etc.

1. INTRODUCTION

The radome CAD modeling in the complex antenna systems is an important process [1, 2], especially in the cases of communication systems with limited power resources (e. g. DBS TV reception). The modern single- and multi-layer radome materials are more or less anisotropic and therefore the radome design becomes enough complicated task [3].

A key circumstance for the accurate RF design of the composite radomes is the right knowledge of the dielectric parameters of the used materials – dielectric constant and dielectric loss tangent of each layer. The most of the modern materials used for the antenna radome fabrications are as a rule anisotropic ones. This means that their dielectric parameters depend on the directions of wave propagation. In the simplest case (one-layer reinforced materials with many penetrating layers) the anisotropy is usually connected with the influence of the supported cloths and fibres, which have different dielectric parameters compared with the filling material. In the case of multi-layer radomes, the anisotropy is a natural property – the dielectric parameters differ considerably for the skins and honeycomb, foam, 3D-glass cores, etc., which usually form non-penetrative layers [4]. Finally, some radomes may have special geometrical forms, which itself caused an additional dielectric anisotropy [5].

The main goals of the contribution are: to present an analytical model of flat multi-layer radome structure taking into account the material anisotropy, to combine this model with a measurement method for accurate determination of the dielectric constant and dielectric loss tangent anisotropy, and finally, to construct practical radome models including all the anisotropic layers in the sandwich composite structure.

2. CAD RADOME MODEL WITH ANISOTROPIC MATERIALS

We accept the geometrical construction and parameter denotations in the plane multi-layer radome structure considered by Paris [1] – Fig. 1. Let the radome consists of $N-1$ non-penetrative layers with a pair of complex relative dielectric constants: $\epsilon_{i,\parallel} = \epsilon'_{i,\parallel} (1 - j\tan\delta_{i,\parallel})$ – parallel to the surface (in the plane Oxy) and $\epsilon_{i,\perp} = \epsilon'_{i,\perp} (1 - j\tan\delta_{i,\perp})$ – normal to the surface (along the Oz axis) ($i = 2, 3, \dots, N$). The layers $i = 1, N+1$ are assumed to be free space. We consider traveling plane wave from left to right (i.e. along the Oz axis), which incident on the radome top skin at an incident angle θ_1 . As a result, four tangential wave field components appear at each i -th interface: two incident ones A_i, A_{i+1} , and two reflected ones B_i, B_{i+1} . The corresponding angles of refraction θ_i and θ_{i+1} could be determined from the simple extension of Snell's law in the case of anisotropic layers, namely,

$$\cos \theta_i = \sqrt{1 - (\epsilon_{1,\parallel} / \epsilon_{i,\parallel})^2 \sin^2 \theta_1}. \quad (1)$$

In general, we consider the radome structure dependently to the electric field orientation of the incident wave in the plane Oxy , i.e. for normal or parallel polarization. Following the analytical procedure described in [1] we can obtain recurrent relations for the tangential field components at each i -th interface surface and finally, we can express the transmission and reflection losses of the multi-layer antenna radome.

Further we present in this contribution the analytical expressions for the case of normal polarization only (see [4] for more details). In this case the electric field component E_x is normal to the incident plane Oyz . If A_i and B_i represent the incident and reflected component E_x at the i -th interface, we can write the following relations:

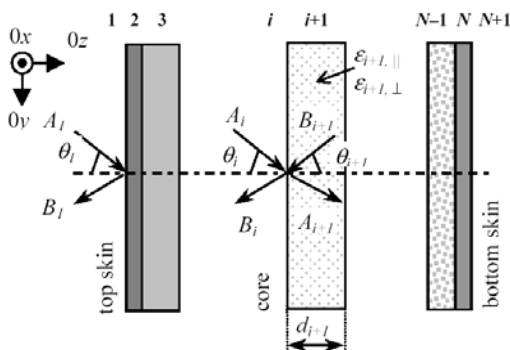


Fig. 1. Multi-layer radome configuration for incident plane wave from left to right

$$A_i = \frac{1}{2} \exp\left(j \frac{2\pi d_i}{\lambda} \sqrt{\varepsilon_{i,\perp}} \cos \theta_i\right) \times [A_{i+1}(1 + Y_i) + B_{i+1}(1 - Y_i)], \quad (2)$$

$$B_i = \frac{1}{2} \exp\left(-j \frac{2\pi d_i}{\lambda} \sqrt{\varepsilon_{i,\perp}} \cos \theta_i\right) \times [A_{i+1}(1 - Y_i) + B_{i+1}(1 + Y_i)], \quad (3)$$

where

$$Y_i = (\cos \theta_{i+1} / \cos \theta_i) \sqrt{\varepsilon_{i+1,\parallel} / \varepsilon_{i,\parallel}}. \quad (4)$$

If we consider a receiving antenna (the top skin is $i = 2$; the bottom skin is $i = N$), we start with $A_{i+1} = 1$ and $B_{i+1} = 0$ and finish with expressions for the E_x components in the layer $i = 1$, i. e. A_1 and B_1 . Finally, we express the insertion IL and return losses RL as follows:

$$IL^{\text{NP}} = 20 \log \frac{1}{|A_1|}, \text{ dB}; \quad RL^{\text{NP}} = 20 \log |B_1|, \text{ dB}. \quad (5)$$

3. RADOME MEASUREMENTS

The measurement of antenna radomes means the experimental determination mainly of the own insertion losses IL , but also the insertion phase IPh and the return losses RL caused by the radome, which cover the antenna. The most popular method for determination of the radome insertion losses is the comparison of the received signals by the antenna with and without radome at the same conditions. This method represents exactly the real antenna environment, but it can be implemented only for *already* manufactured radome. In many practical cases (for example, communication systems with very critical parameters) this method is expensive and ineffective. The other known method is measurement of the radome-wall parameters by the free-space method. The measurement setup consists of two well-matched antennas (usually horns) installed at large enough distance from the radome sample ($\sim 10\lambda_0$), thus ensuring far-field plane-wave behavior of the system [6]. This method is also more or less inconvenient, because it requires large radome samples. The sample dimensions can decrease, if spot-beam antennas are used (spot-focusing lens horns, distance $\sim 3\lambda_0$). Two main sources of errors are typical for these measurement systems – diffraction effects from the specimen edges and multiple reflections. The main advantage of the free-space method is the possibility to control and to change easily the incident angle θ , which is important in the case of radome measurements. The near-field methods are another methods employed for radome test – utilization of small samples inserted into waveguides, coaxial lines, etc. Two methods are well known – transmission-type measurements between two open-end waveguides [7] and reflection-type measurements by open-ended coaxial probes, when the other end of the sample is well grounded [8]. The main problem of the considered methods is that the measurement in case of very small radome losses is inaccurate and irreproducible and needs special calibration procedure. Another problem is that the incident angle could not be changed.

We propose rather different procedure for radome characterization. First of all, we accurately determine the full set of the dielectric parameters of the all radome layers using small samples (see Part 5) measured by a resonance method. Then, we construct a realistic radome composition, comprising all layers and finally, apply an analytical model for calculation of the radome insertion losses, insertion phase and return losses (see the example in Part 6).

4. RADOME SIMULATIONS

The antenna radome simulations by 3D electromagnetic simulators are not an easy task due to the large-scale models, compared with the wavelength. The problems are practically the same as in the similar free-space measurement set-ups – the antenna radome specimen should be big enough in order to avoid the diffraction effects. Therefore, the structures under simulation become usually large than $(5-6)\lambda_0$, which leads to large memory requirements and the CPU time becomes impractically long.

First, we present in Fig. 2 the 3D model of a “close-to-reality” structure: a radome specimen between two open-end waveguides at incident angle 45 deg, placed in a PML (perfectly matched layer) box. The picture represents a 1/2-symmetrical part of the whole structure and shows the E-field distribution in several cuts. One can see the main E-field spot concentrated in the sample center, but along with other relatively high level local diffraction maximums that also are observed in the sample. Therefore, the calculated S parameters (e.g. IL) are not very realistic even at appropriate meshing ($> 10^5$ tetrahedra).

To avoid these problems we construct a less realistic structure, however more suitable for 3D simulations – Fig. 3. It consists of a radome sample with smaller dimensions in PML box, illuminated by plane wave with normal or parallel polarizations at different incident angles. Now the S parameters could not be directly obtained, however the values of the Pointing vectors can be evaluated at two specific planes – P1 (input) and P2 (output) after integration. Thus, if we compare these integral values at plane P2 in structure with and without radome, the own insertion losses IL can be easy determined.

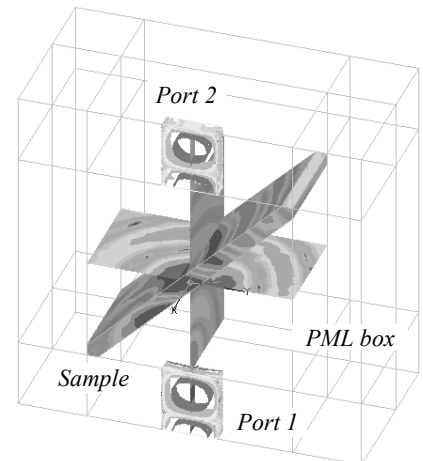


Fig. 2. 1/2 part of a large simulated structure: radome sheet between two open-end waveguides

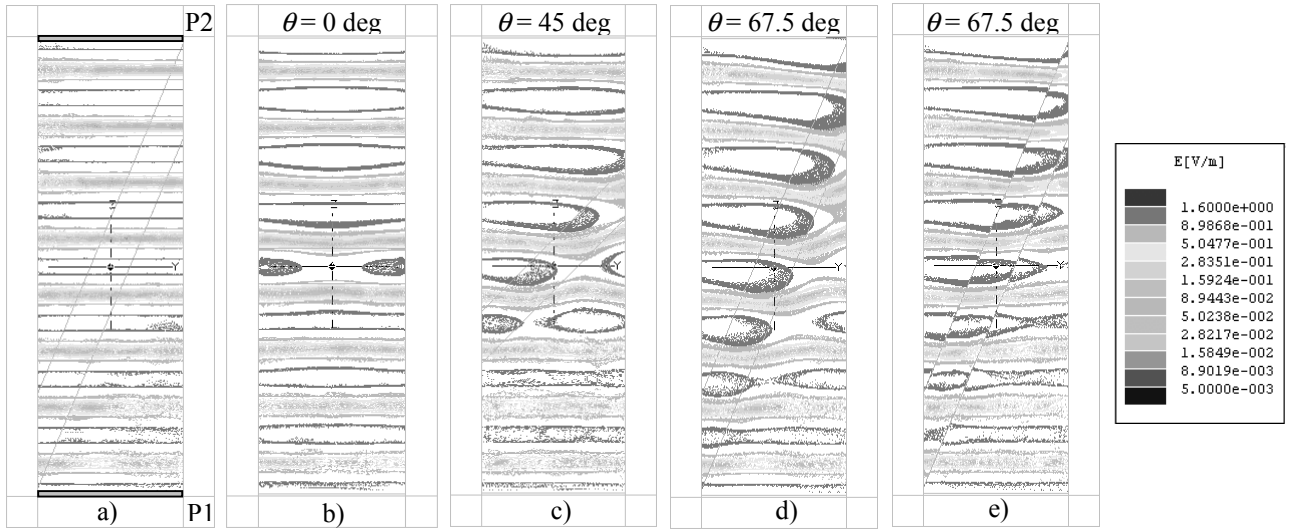


Fig. 3. Incident (a) and total E field in PML box with radome, illuminated by plane wave – normal NP (b, c, d) and parallel PP (e) polarization

5. CHARACTERISATION OF THE MULTI-LAYER MATERIALS AND RADOME MODELING

We have proposed an accurate measuring method (called two-resonator method) for determination of the material anisotropy [3, 9]. This method is based on determination of the longitudinal parameters (parallel to the surface plane) by cylindrical TE_{011} -mode resonator and the transversal parameters (normal to the surface plane) by cylindrical TM_{010} -mode resonator – Figs. 4, 5. The main advantage of this method is the possibility to obtain full set of the dielectric parameters (dielectric constant and loss tangent) of each layer in the multi-layer samples (from the composite antenna radome), if the other layers have known parameters. This "extraction procedure" allows accurate determination of the dielectric anisotropy even of layers, which could not form self-depending samples (thin coating, different radome cores, e.g. 3D-glass cores, etc.) and to be directly measured.

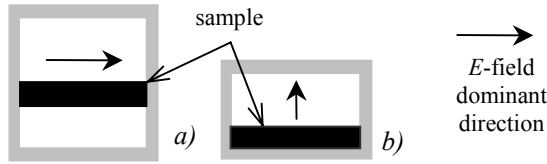


Fig. 4. a) TE_{011} -mode cavity **R1**; b) TM_{010} -mode cavity **R2**

We present in Table I the measured parameters of one concrete material used as radome at 12.5 GHz – Parabeam® 3D-glass fabrics with specific vinyl-ester resin. Two types of data are shown here: 1) for a single-layer structure (*average sample*) and 2) for three-layer sample with different top and bottom skins and irregular core (3D glass filling) – Fig. 6. Thus, we can construct two different radome models. The simplest Model 1 is a single-layer construction with not so big anisotropy $\Delta A_\epsilon \sim 6.1\%$, $\Delta A_{\tan\delta\epsilon} \sim 38.6\%$ ($\Delta A_\epsilon = 2(\epsilon'_{\parallel} - \epsilon'_{\perp}) / (\epsilon'_{\parallel} + \epsilon'_{\perp})$ is the dielectric-constant anisotropy and $\Delta A_{\tan\delta\epsilon} = 2(\tan\delta_{\epsilon\parallel} - \tan\delta_{\epsilon\perp}) / (\tan\delta_{\epsilon\parallel} + \tan\delta_{\epsilon\perp})$ is the loss-tangent anisotropy). The more realistic radome Model 2 is 3-layer construction with two skins and core. According to the presented results, the both skins are strongly anisotropic (especially the bottom skin due to the air balloons included). The core is strongly irregular, but less anisotropic. The core could not be directly measured as a separate layer; its dielectric parameters can be obtained only after an "extraction procedure", described in [9]. It is important to note that the dielectric constant and the loss tangent in the separate layers have bigger values along to the directions *parallel* to the woven glass fibres. As a result, the both constructed models show different behaviour of the considered antenna radome, especially for the insertion losses – see the example, described in the next section.

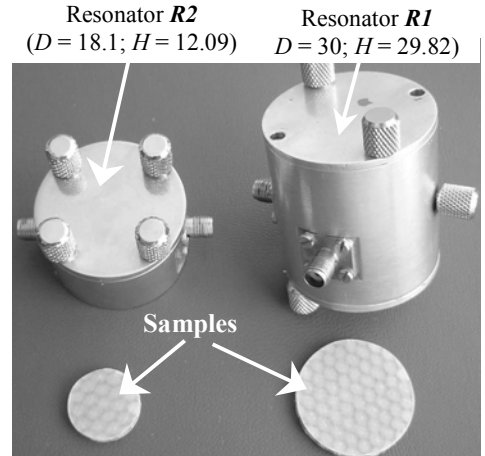


Fig. 5. Photograph of the both measuring resonators with corresponding radome samples; D, H in mm

TABLE I
CHARACTERIZATION OF MULTI-LAYER PARABEAM® 3D-GLASS FABRICS RADOME ([HTTP://WWW.PARABEAM.NL/](http://www.parabeam.nl/))

Antenna-radome layers	d_i , mm	ϵ'_{\parallel}	ϵ'_{\perp}	$\tan\delta_{\epsilon\parallel}$	$\tan\delta_{\epsilon\perp}$	ΔA_ϵ , %	$\Delta A_{\tan\delta\epsilon}$, %
• Radome Model 1 (one average layer) (frequency range ~12.5 GHz)							
1.0 Average sample	7.75 ± 0.05	1.375	1.294	0.0071	0.0048	6.1	38.6
• Radome Model 2 (three layers) (Dion 9100 – M700; vinyl ester resin)							
2.1 Top skin layer (smooth epoxy glass+ clothes)	0.52 ± 0.05	3.49	2.66	0.015	0.013	27.0	14.3
2.2 Core (irregular 3D glass filling)	6.76 ± 0.10	1.163	1.230	0.0039	0.0045	-5.6	-15.8
2.3 Bottom skin layer (rough epoxy glass + clothes)	0.47 ± 0.05	2.72	1.75	0.015	0.0047	45.6	104.6

6. PRACTICAL EXAMPLE – PARAMETERS OF PARABEAM® 3D GLASS RADOME

We present in this section a short example – comparison between the calculated and measured insertion losses IL in Parabeam® 3D-glass radomes in the frequency range 9-15 GHz. First of all, the calculated IL dependencies versus the incident angle θ at fixed frequency (Fig. 7a) and versus the frequency at fixed θ (Fig. 7b) (normal polarisation NP) are given. The analytical expressions (5) are applied for the both radome models 1 and 2 in accordance with the layer dielectric parameters in Table I. We compare the results for the following four cases – for 1-layer or 3-layer radome models and for anisotropic or isotropic materials. The 3-layer model was found to be more accurate – it gives smaller IL than the values obtained by 1-layer model (e.g. twice at $\theta = 45$ deg). The HFSS simulations at fixed angles (0, 45, 67,5 deg – see constructions on Fig. 3) fully confirm the values from the analytical approximation. The radome modeling with anisotropic or with isotropic materials is also important. Calculation errors in the isotropic case may appear, if we use parallel or normal dielectric parameter only (depending of the measuring method) – see comparison in Fig. 7a. The experimental results for IL , especially at big incident angles (see Fig. 7b) are in a very good accordance (<10 %) with the analytical data obtained by 3-layer radome model with anisotropic material parameters. Our older investigations have shown that in case of thick resonance radome constructions (see [4]) the influence of the material anisotropy is even considerable bigger.

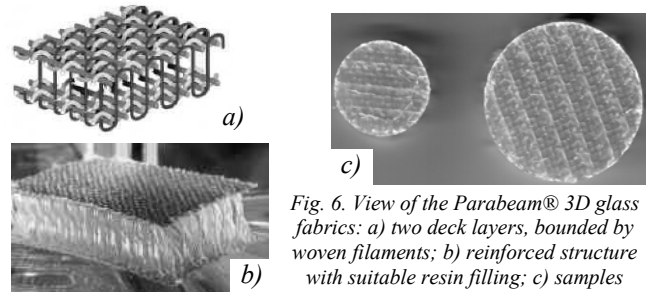


Fig. 6. View of the Parabeam® 3D glass fabrics: a) two deck layers, bounded by woven filaments; b) reinforced structure with suitable resin filling; c) samples

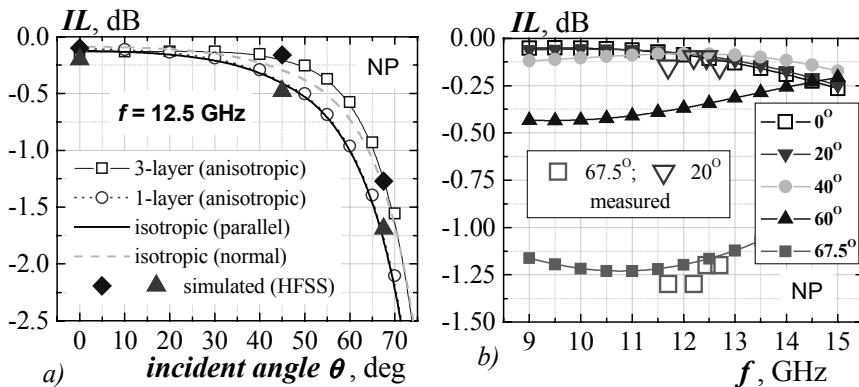


Fig. 7. Dependencies of the insertion losses IL in Parabeam® 3D glass radome with dielectric parameters, given in Table I:

a) versus the incident angle at 12.5 GHz (Model 1 and Model 3)

b) versus the frequency at several incident angles (Model 3)

The results are compared with Ansoft® HFSS simulations for 1-layer and 3-layer anisotropic radome models. The measured data are obtained by measurement of the received signal in DBS-TV stirable antenna array with and without covering radome.

7. CONCLUSIONS

This paper is an attempt to combine analytical CAD radome models taking into account the layer dielectric anisotropy with a test method (two-resonator method) for more precise characterisation of the layer dielectric parameters in the both directions – normal and parallel to the radome surface. As a result, practical enough and useful radome models in each concrete case could be introduced, where the particular contribution of each layer appeared in the radome construction – cores, skins, irregular epoxy glue fillets, 3D-glass fabrics, protective coatings, etc., can be effectively represented. Some of these layers could not be measured directly, which makes the proposed extraction procedure very attractive exactly for radome applications.

8. ACKNOWLEDGEMENT

The authors thank to Scientific Research Found of University of Sofia “St. Kliment Ohridski” and to RaySat BG for the preliminary support.

9. REFERENCES

- [1] D. T. Paris, “Computer-Aided Radome Design”, *IEEE Trans. Antennas Propagat.*, AP-18, Jan. 1970, pp. 7-15
- [2] D.J. Kozakoff, “Analysis of Radome-Enclosed Antennas”, Artech House Inc., 1997, Ch. 5
- [3] Plamen I. Dankov, “Two-Resonator Method for Measurement of Dielectric Anisotropy in Multi-Layer Samples”, *IEEE Trans. on Microwave Theory and Tech.*, MTT-54, April 2006, pp. 1534-1544
- [4] Vesselin N. Peshlov, Plamen I. Dankov, Boyan Hadjistamov, “Models of Multi-layer Antenna Radomes with Anisotropic Materials”, *1st European Conference on Antennas and Propagation EuCAP’2006*, France, Nice, November 2006, No. 349840PD (available IEEE X-plore)
- [5] D. G. Bodnar and H. L. Bassest, “Analysis of an Anisotropic Dielectric Radome”, *IEEE Trans. Antennas Propagat.*, AP-23, pp. 841-846, 1975
- [6] J. D. Mahony, “Measurements to Estimate the Relative Permittivity and Loss Tangents of Thin Low-Loss Materials”, *IEEE Antennas & Propagat. Magazine*, vol. 47, No. 3, June 2005
- [7] M. E. Baginski, D. L. Faircloth and M. D. Deshpande, “Comparison of Two Optimization Techniques for the Estimation of Complex Permittivities of Multilayered Structures Using Waveguide Measurements”, *IEEE Trans. on Microwave Theory and Tech.*, MTT-53, No.10, Oct. 2005, pp. 3251-3259
- [8] A P Gregory, R N Clarke, T E Hodgetts and G T Symm, “RF and Microwave dielectric measurements upon layered materials using coaxial sensors”, NPL Report MAT 13, February 2008
- [9] Plamen I. Dankov, Valda P. Levcheva and Vesselin N. Peshlov, “Utilization of 3D Simulators for Characterization of Dielectric Properties of Anisotropic Materials”, *35th European Microwave Conference EuMW’2005*, Paris, France, Oct. 2005, pp. 517-520

COLUMBUS/ISS CP DUAL-BAND, SLIM ANTENNAS MADE WITH A COMPOSITE MULTI-LAYER PANEL

Pawel Kabacik⁽¹⁾, Grzegorz Jaworski⁽¹⁾, Monika Hornik⁽¹⁾, Tomasz Maleszka⁽¹⁾,
Przemyslaw Gorski⁽¹⁾, Damian Wydymus⁽¹⁾

⁽¹⁾ Institute of Telecommunications, Teleinformatics and Acoustics
Wroclaw University of Technology, 50-370 Wroclaw, Poland
<http://www/zitim.pwr.wroc.pl> Email to the authors: first_name.name@pwr.wroc.pl

Abstract: The paper presents a pair of microwave lightweight slim antennas for installation on Meteorite Debris Panels of the Columbus laboratory which is a part of the International Space Station (ISS). The single-fed antenna operates at two radioamateur bands: 1260-70 MHz and 2400-50 MHz. The antenna composite panels have 9.9 mm thickness and had been manufactured with a technology of sophisticated multilayer composites. Advance materials and design methods were applied and thus, the antenna structure has been capable to meet extremely severe requirements due to launch loads and to harsh space environment. Owing to advantageous features of the developed composite antennas, their installation was possible on Earth – thus saving considerable efforts unavoidable during installation works at EVA.

1. Introduction

The research presented in this paper had aimed at development of low-profile dual-band antenna for installation on an outer surface of the Columbus laboratory – a main ESA contribution to the ISS. The antenna has to meet extremely strict requirements of space approval applicable for transportation to the orbit on the outside side of the Columbus [1], [2]. Needless to say that antennas are to operate in harsh low orbit environment for many years. Furthermore, extremely demanding conditions are due to use at manned space flights. Two identical antennas were installed on Columbus to ensure redundancy. Originally antenna applications were limited to planed digital radioamateur services which are operated at the ISS under the organization Amateur Radio on International Space Station (ARISS). Antennas are a core part of presently being developed ARCOL radioamateur station on the ISS, however, their discussed applications go beyond ARCOL, as operational frequency ranges are broader.

2. Developed Composite Antennas for the Columbus laboratory at the ISS

To survive severe launch loads antennas must be extremely strong and do not produce excessive loads to the spacecraft. For these applications, composite structures made with low weight cores and strong bonding layers are potentially suitable. Nowadays modern materials make feasible development of such strong structure capable to sustain great temperature extremes. However, to formulate a short list of potentially useful materials extensive studies must be performed over considerable time period - a year or longer. Apart electrical properties at microwave frequencies, several classes of problems must be taken in considerations: thermal, outgassing, immunity to atomic oxygen and resistance to space radiation. Actual thermal properties must be carefully verified against

temperature cycles required during technological processes (i.e. how different are actual thermal expansion effects during curing).

In our antennas, the composite panel has ~10 mm thickness, depending on a concept has between 12 and 19 layers in multilayer composite panel, as it can be seen in Fig. 1 revealing a simplified cross-section of one of composite panels investigated in a course of our research. Extrusion of the antenna above Columbus outer surface varies and the greatest extrusion approaches 30 mm at edges.

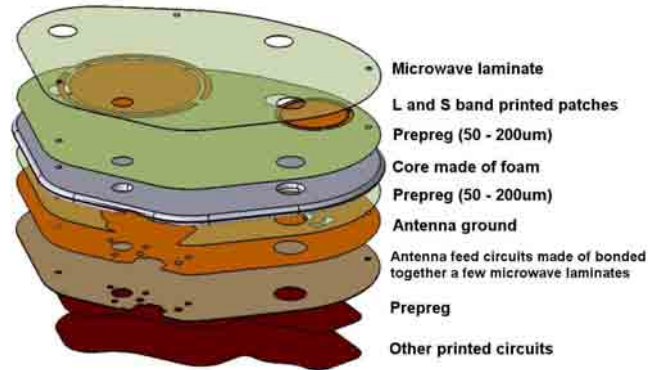


Fig. 1. Major layers in the antenna composite panel.

Two quite different antennas prototypes are shown in Fig. 2 – one of them is shaped cylindrically and conforms to a cylindrical surface of the Columbus. At the upper antenna side there are two circularly polarized patches – one for the L-band and another one for the S-band. Patches are coupled to feed lines and their circular polarizers through a pair of C-slots [3], [4]. The single-fed antenna operates at two radioamateur bands: 1260-70 MHz and 2400-50 MHz. At the bottom antenna side there is a microwave feed circuit. Figure 3 presents photographs of the flight antenna at both sides. Wireline sketch of printed circuits arranged on several layers in the antenna is depicted in Fig. 4. Polarizers needed to generate circular polarization are made with three-strip directional couplers [5], [6]. The feed is complemented with a diplexer which is made with impedance traps.

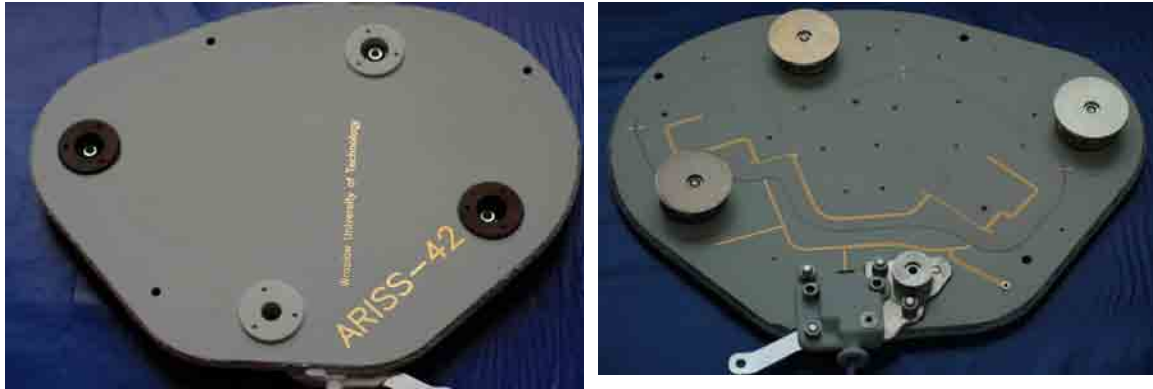


(a) cylindrical side profile



(b) planar side profile

Fig. 2. Two manufactured prototypes of antennas which differ significantly in their layer arrangement of composite panels and side profile.



(a) patches seen at the front view

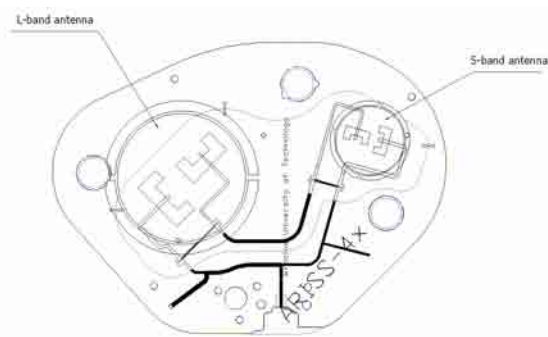
(b) back view with a feeding network

Fig. 3. Front and back side view of one of flight antennas.

The antennas were mounted on the ESA Columbus laboratory at NASA Kennedy Space Center in 2007. Antennas mounted on the Columbus are shown on photographs in Figs. 5 and 6. The laboratory was delivered to the International Space Station (ISS) during the STS-122 US *Atlantis* space shuttle mission and commissioned in February 2008.

3. Antenna Performance

A few series of different antenna models were manufactured in groups of three to five identical pieces. In this paper properties of developed antennas are discussed from impedance points of view. Due to a high degree of integration and complex nature of glued core structures, antenna impedance properties were measured for the fully assembled antennas at a feed point. Microwave feed components were manufactured and measured – examples of results are plotted in Fig. 7. However results of these tests should be regarded as a certain contribution to gradual evaluation of antennas featuring a high degree of integration. The antenna cable input made infeasible soldering of a connector, as it was made in a way a microwave cable must be connected by clamping. Thus impedance match had to be measured with a short cable section connected to the antenna input. In our antennas measured return loss approached 21 dB at best values and generally were not worse than 13 dB. One of the measured return loss characteristics is plotted in Fig. 8. In all microwave antennas made with composite panels, electrical characteristics of materials used in the panel, have paramount impact on radiation capabilities, antenna gain and losses.



Transparent view through ARISS-4x printed circuit (view from the top)

Fig. 4. Transparent wireline drawing of antenna element and feed circuit placed on four printed circuit layers.



Fig. 5. One of the flight antenna installed on a Meteorite Debris Panel of the Columbus laboratory.



Fig. 6. Columbus laboratory ready for loading into a cargo bay of *Atlantis* US space shuttle. Two ARISS antennas are clearly visible in the upper part of the Columbus.

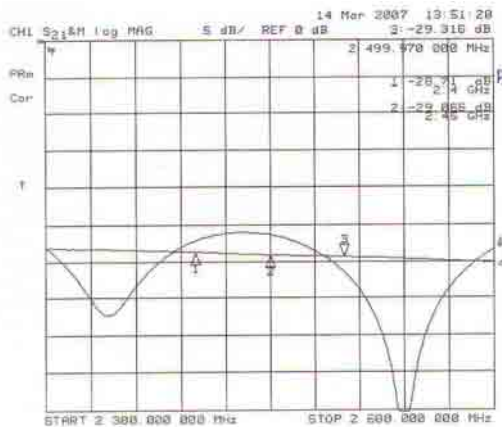


Fig. 7. Measured frequency characteristics of a model of the S-band three-strip directional coupler.

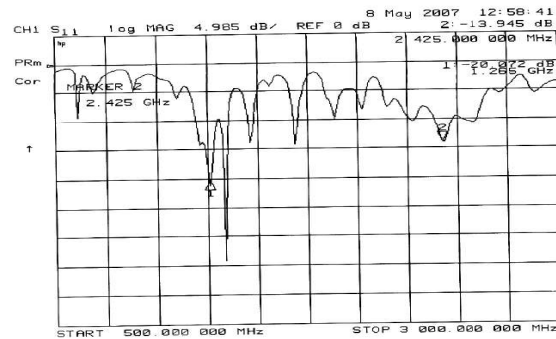


Fig. 8. Measured return loss of one of the antenna prototype.

4. Conclusions

Use of multilayer composite structures in antennas installed on spacecraft is nowadays particularly attractive when spacecraft is small to medium size or when there are volume

limitations set to a stowed spacecraft by a launch vehicle. Further advantages of slim multilayer antenna panels are expected to become of primary importance when use of advanced beamforming techniques will become more feasible onboard spacecraft.

The development of the Columbus/ISS slim antennas with a composite multi-layer panel was a big challenge. Carefully designed lightweight antenna elements and their feed utilizing coupled lines arranged on a dual-layer printed circuit had set a lot of specific challenges to mechanical, thermal and material issues. They have been identified in a course of examination several engineering models and thoroughly addressed. To find fully satisfactory responses to all these “other-than-electromagnetic-nature” problems, a two-year intensive studies performed by a dozen institutions and another dozen of material producers were required. The developed antenna meets strict requirements of launch conditions and can sustain long term use in the space environment on the ISS orbit. The accomplished research has produced a lot other interesting major results on composite antennas – just to mentioned some – a few considerable different prototypes were manufactured and tested. The gained knowledge should make faster and easier design of other antennas for uses in challenging applications including aerospace, trains, vessels.

Acknowledgment. The authors thanks to ESA, NASA, international organization ARISS, Ministry of Sciences and Higher Education, Republic of Poland, EADS Astrium, Thalesaleniaspace, AOES and a dozen other companies/space qualified laboratories for securing funding and for significant contributions to development of the described composite antennas.

References

- [1] P. Kabacik, G. Jaworski, M. Hornik, „Small spaceborne microstrip antennas,” *29th ESA Antenna Workshop on Multiple Beam and Reconfigurable Antennas*, ESTEC, Noordwijk, 18-20 April 2007.
- [2] P. Kabacik, G. Jaworski, M. Hornik, T. Maleszka, „Lightweight L- and S-Band Antenna Fed by Three-Strip Directional Couplers,” *2007 IEEE Antennas and Propagation Society International Symposium*, Honolulu, Hawaii, June 10-15, 2007.
- [3] M. Hornik and P. Kabacik, „ Investigations into Lightweight Patch Element for Use in Dual- or Multi-Polarized Antenna Arrays,” *2007 IEEE Antennas and Propagation Society International Symposium*, Honolulu, Hawaii, June 10-15, 2007.
- [4] M. Kamaszuk, P. Hornik, D. Guzda, P. Kabacik, “Optimizing circular polarization within a beam of patch antenna elements,” *Journal of Telecomms and Information Technology*, No. 1, 2007.
- [5] K. Sachse and A. Sawicki, “Quasi-ideal multilayer two- and three-strip directional couplers for monolithic and hybrid MIC,” *IEEE Trans. on MTT*, vol. 47, no. 9, pp. 1873-1882, Sept. 1999.
- [6] M. Bona, L. Manholm, J. P. Starski, B. Svensson, “Low-Loss Compact Butler Matrix for a Microstrip Antenna,” *IEEE Trans. on MTT*, vol. 50, no. 9, pp. 2069-2075, Sept. 2002.

A COMPACT AND LOW COST RADIATING ELEMENT FOR AUTOMOTIVE SATELLITE BROADCASTING RECEPTION ARRAYS

Roberto Torres-Sánchez⁽¹⁾, Stefano Vaccaro⁽²⁾, Juan R. Mosig⁽¹⁾

⁽¹⁾EPFL-LEMA, LEMA-ELB-EPFL-Station 11, CH-1015 Lausanne, Switzerland, roberto.torres@epfl.ch

⁽²⁾JAST SA, PSE-EPFL Bat. C, CH-1015 Lausanne Switzerland, stefano.vaccaro@jast.ch

INTRODUCTION

ESA-ESTEC has launched its project NATALIA (New Automotive Tracking Antenna for Low-cost Innovative Applications [1]) to cope with the current and ever increasing requirements in terms of performance, cost and aesthetics that novel applications are demanding in the field of consumer satellite communications. NATALIA requires a low profile electronically steerable Ku-band phased array with polarization tracking capabilities and with a surface close to that of a Compact Disc. A typical application scenario is depicted in Fig. 1 (courtesy of the NATALIA project team). This paper presents a multilayered patch antenna conceived to be the basic radiating element for such an array.

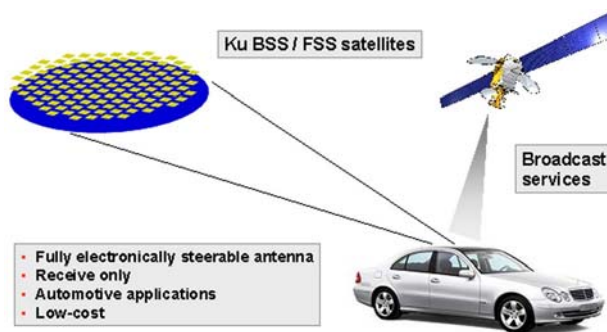


Fig. 1. NATALIA example

DESIGN

After a thorough evaluation of the current technological possibilities and of their capability to match the requested specs, the multilayer printed circuit technology has been selected as the preferred choice for the whole antenna array. This technology is very well suited for mass-production, intrinsically compatible with streamlined geometries and mature enough to afford demanding professional applications. As a consequence, the radiating element is a inverted microstrip patch antenna with dual linear polarization fed by apertures coupling from striplines (Fig. 2). Similar ideas can be found in the literature, including previous designs by LEMA-EPFL [2], [3], [4], [5].

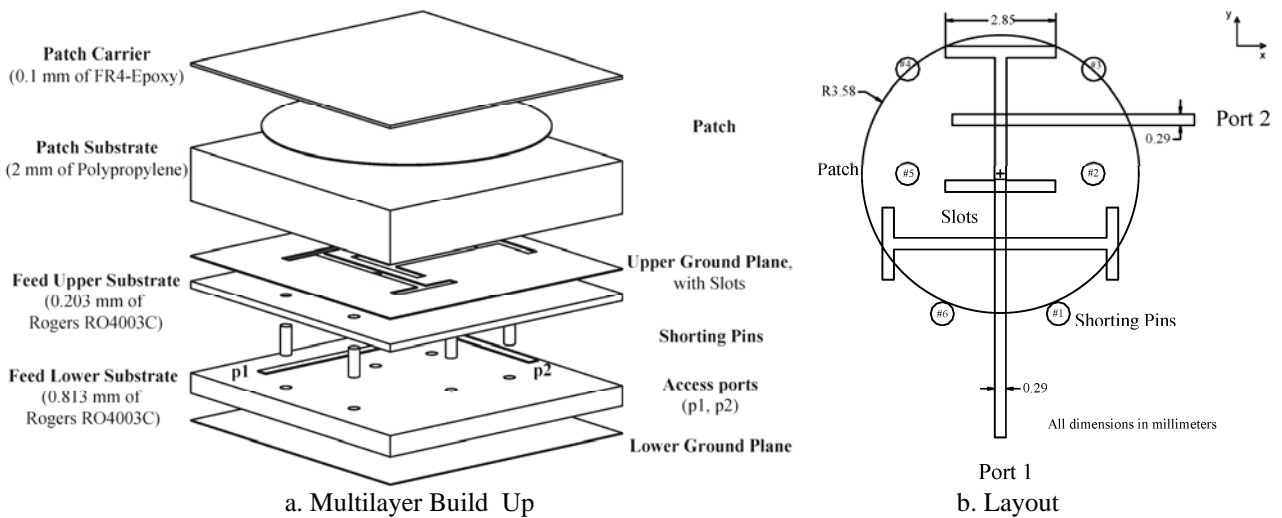


Fig. 2. Radiating Element Structure

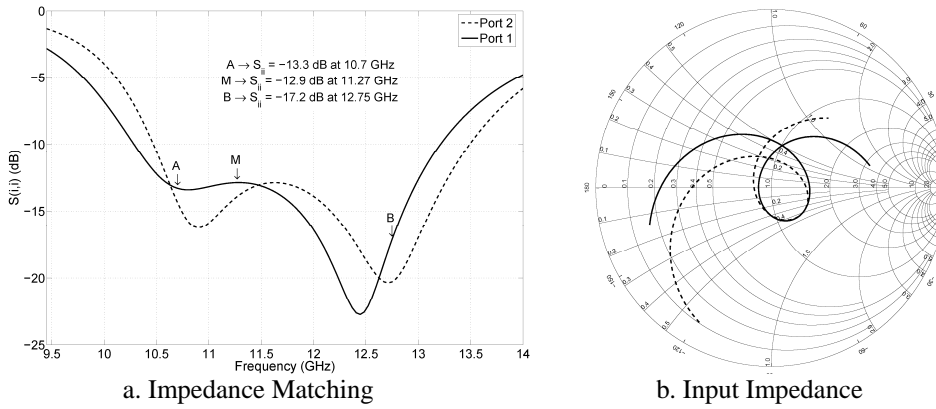


Fig. 3. Reflection coefficients of the radiating element

The basic multilayer structure of the radiating element is composed by four metallization layers (the patch, the slotted ground plane, the feeding lines and a shielding bottom ground plane), three kinds of dielectric materials (epoxy, polypropylene and Rogers RO4003C™) and six metallic posts (shorting pins), which vertically cross part of the stack to connect both ground planes.

An important advantage of the microstrip aperture coupled architecture is the separation provided between the radiation and the feeding of the radiating element. But this design requires a new shielding layer to prevent possible undesired back radiation towards a shared multilayer stack-up, where all the phased array logic is going to be embedded. Such shielding layer is going to be provided by the bottom ground plane. In this way, the feeding of the radiating element is no longer microstrip-like. Rather, being confined between two ground plates, it becomes a sort of stripline. Therefore, special attention must be paid, on one side to provide a proper coupling between the feeding lines and the patch trough the slot and, on the other hand, to mitigate as much as possible the power leakage due to the parasitic parallel plate waveguide modes. These modes can be excited due to the asymmetry introduced by such slots. These two issues are taken care of, firstly by making the stripline asymmetric (with the lines closer to the slotted ground plane), which provides a proper coupling between the feeding lines and the slots and, secondly by carefully placing six metallic posts around the slots which will short-circuit the most dangerous parallel plate waveguide mode, in a way inspired by [5].

The electromagnetic modelling, design and optimisation of the radiating element has been done following the guidelines presented in [5], [6], [7], using full wave simulation tools either commercial (Ansoft's Designer and HFSS) or home made codes (IE-MoM). As shown in fig. 3, these tools predict a proper impedance matching ($|S_{ii}| \leq -12.9\text{dB}$ between 10.7GHz and 12.75GHz, $|S_{ii}| \leq -10\text{dB}$ over a relative bandwidth of 23%) and a port decoupling better than 40dB. The simulation also shows very promising levels of radiation efficiency (over 75%, thanks to an appropriate placement of the shorting pins), symmetry of the radiation diagrams, good polarization purity (with a crosspolar component 18dB below the broadside copolar level) and adequate directivity (between 7.5dB and 8.2dB) over the whole frequency band of interest.

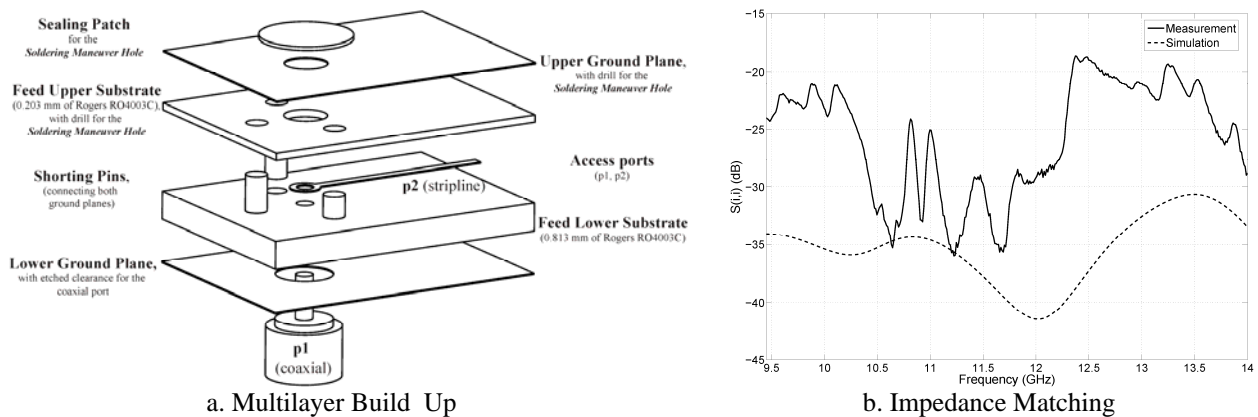


Fig. 4. Stripline to coaxial transition

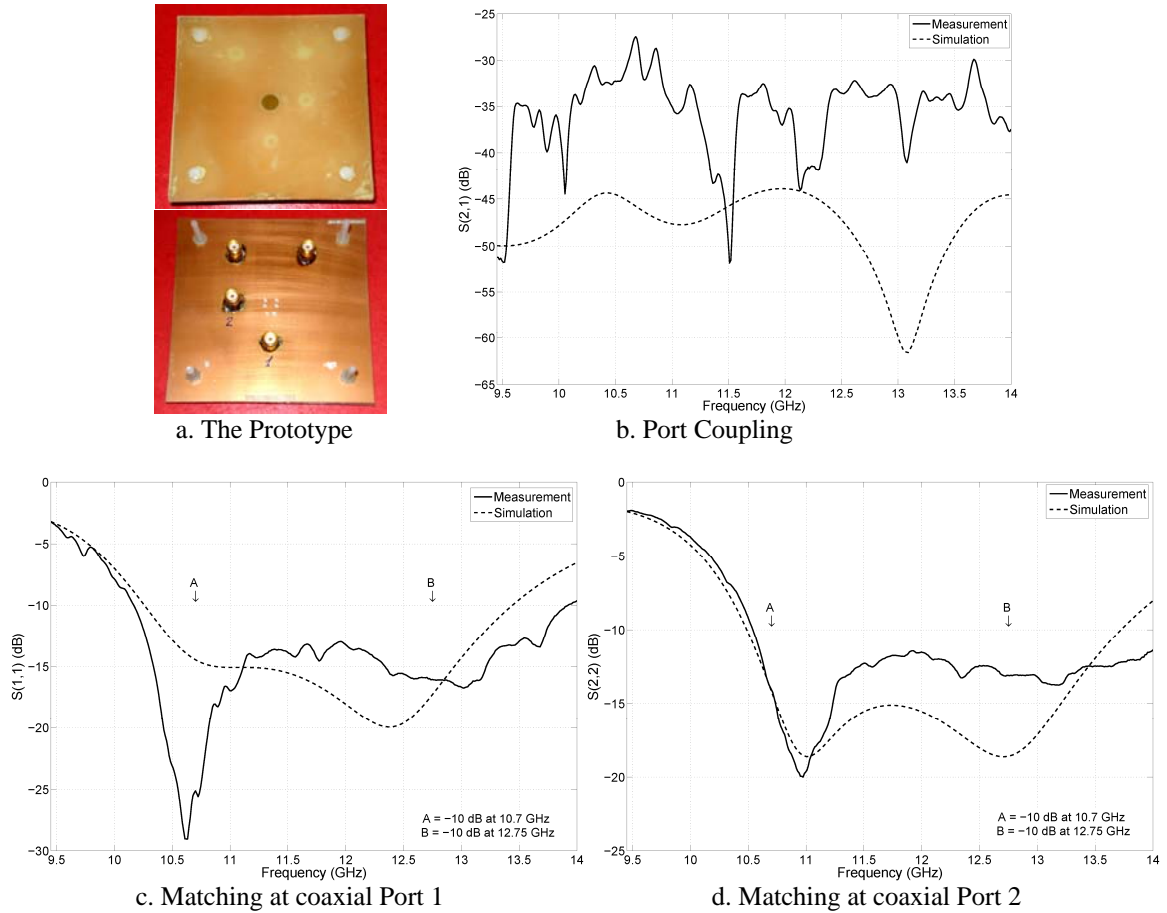


Fig. 5. The fabricated prototype and its Scattering parameters

IMPLEMENTATION AND RESULTS

In the practical implementation and prototyping of the radiating element, a cornerstone problem is to ensure proper and well matched transitions between coaxial and stripline lines. To this end, the access to the stripline ports of the radiating element is done through dedicated shielded miniature right angle coaxial to stripline transitions, whose structure is shown in Fig. 4(a) and which are designed to provide correct levels of transmission losses and of impedance matching. The average measured values for the losses in the working frequency band of 10.70-12.75 GHz oscillates between 0.24dB and 0.30dB, in good agreement with predicted results. As for matching, it remains better than 20dB in the same frequency band of interest (see Fig. 4b).

A prototype of the radiating element was built (see Fig. 5a) and its performance was characterized. Measured results show good agreement with predicted values, both in terms of scattering parameters and radiation diagram, as displayed in Figs. 5b, 5d and 6. The quality of the linear polarization, with a very reduced crosspolar component (below -20dB) for both ports all over the frequency band of interest, is considered to be particularly promising as suggested by Fig. 6 (where only results for port 1 are shown, since the radiation diagrams corresponding to both ports are very similar).

The observed agreement between the predicted behaviour for the radiating element and the measured results provides an empirical assessment of the validity of the proposed radiating element concept and of its performance, as well as a good check of the quality and accuracy of its electromagnetic modelling.

CONCLUSION

In this paper, a very promising radiating element for low cost automotive satellite reception has been presented. Such element is an inverted microstrip patch antenna with dual linear polarization fed by striplines coupling through apertures. The stripline feeding of the element makes it suitable for integration in a planar multilayered system, as the NATALIA phased array, but calls for special techniques to prevent performance degradation due to parallel plate parasitic modes. These requirements have forced us to develop dedicated coaxial-to-stripline transitions of very good quality. The finally proposed radiating element has been built and measured, thus providing an empirical assessment of the proposed feeding concept, of the element itself and of its performance.

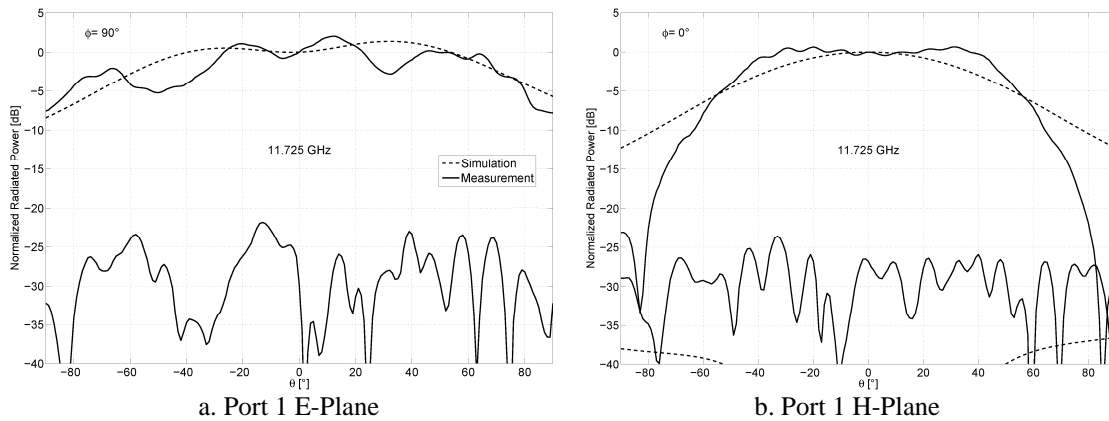


Fig. 6. Elevation Cuts of the radiation Diagram at the central frequency

ACKNOWLEDGMENT

This paper has been done under ESA-ESTEC Contract 18612/04. The authors' institutions are both members of the European COST Action IC0603 "ASSIST" whose support is appreciated. The authors wish to gratefully acknowledge C. Manganot (ESA-ESTEC), D. Llorens del Río (JAST), J.-F. Zürcher (EPFL) and the EPFL Printed Circuits Workshop (EPFL-STI-PAT-ACI) team for their inestimable advise and support on the design and theoretical modelling of the radiating element, as well as on the breadboarding process and on the measurements of the prototypes.

REFERENCES

- [1] R. Baggen, S. Vaccaro, D. Llorens del Río, "Design Considerations for Compact Mobile Ku-Band Satellite Terminals," in *2nd European Conference on Antennas and Propagation, EuCAP 2007*. Edinburgh, UK, Nov. 2007, pp. 1–5.
- [2] D. M. Pozar, "Microstrip antenna aperture-coupled to a microstripline," *Electron. Lett.*, vol. 21, no. 2, pp. 49–50, Jan. 1985."
- [3] J.-F. Zürcher, "The SSFIP: A global concept for high performance broadband planar antennas," *Electron. Lett.*, vol. 24, no. 23, pp. 1433–1435, Nov. 1988.
- [4] D. M. Pozar and S. D. Targonski, "Improved coupling for aperture-coupled microstrip antennas," *Electron. Lett.*, vol. 27, no. 13, pp. 1129–1131, June 1991.
- [5] P. Brachat and J. M. Baracco, "Dual-polarization slot-coupled printed antennas fed by stripline," *IEEE Trans. Antennas Propagat.*, vol. 43, no. 7, pp. 738–742, July 1995.
- [6] P. L. Sullivan and D. H. Schaubert, "Analysis of an aperture coupled microstrip antenna," *IEEE Trans. Antennas Propagat.*, vol. AP-34, no. 8, pp. 977–984, Aug. 1986.
- [7] R. Torres-Sánchez, "Two beam printed antenna array for satellite reception," *Master Thesis (in Spanish)*, Escuela Técnica Superior de Ingenieros de Telecomunicación. University of Málaga. Spain, Mar. 2006. [Online Abstract]. Available: http://www.coit.es/pub/ficheros/p_astra_dfb74c86.pdf